



# The arrest and recession dynamics of a deflating rectangular hydraulic fracture in a permeable elastic medium

Anthony Peirce 

Department of Mathematics, University of British Columbia, Vancouver, BC V6T 1Z2, Canada

**Corresponding author:** Anthony Peirce, [peirce@math.ubc.ca](mailto:peirce@math.ubc.ca)

(Received 6 November 2024; revised 4 July 2025; accepted 11 July 2025)

This paper considers the propagation, arrest and recession of a planar hydraulic fracture in a porous elastic medium whose footprint is constrained to a growing or shrinking rectangular region with a constant height. Hydraulic fractures with large aspect ratio rectangular footprints are frequently referred to as PKN fractures in recognition of the original researchers (Perkins & Kern 1961 *J. Petrol. Tech.* **13**, 937–949) and (Nordgren 1972 *J. Petrol Technol.* **1972**, 306–314) who first analyzed models of such fracture geometries. We investigate the one-dimensional non-local PKN approximation to a fully planar rectangular hydraulic fracture model in a three-dimensional elastic medium. By analysing the tip behaviour of the non-local PKN model, a transformation procedure is established to render the asymptotic equations for the dynamics of the steady semi-infinite PKN and plane strain models formally identical, which implies that all the existing multiscale plane strain asymptotes can be converted directly to the PKN case by making use of this transformation. Using this transformation, it is shown that the appropriate PKN asymptotes for the average aperture  $\bar{w}$  with distance  $\hat{x}$  to the fracture front are  $\bar{w} \sim \hat{x}^{1/2}$ ,  $\hat{x}^{5/8}$  and  $\hat{x}^{2/3}$  in the toughness, leak-off and viscous modes of propagation, respectively; as well as the linear elastic fracture mechanics tip asymptote  $\bar{w} \sim \hat{x}^{1/2}$  for arrest, which transitions to the linear asymptote tip  $\bar{w} \sim \hat{x}$  for a fracture driven to recede due to fluid leak-off. Both the arrest and recession tip asymptotes share the intermediate leak-off asymptote  $\bar{w} \sim \hat{x}^{3/4}$ . A scaling analysis yields the arrest time, length and aperture as functions of a dimensionless injection-cessation time  $\omega$ . An asymptotic analysis of the non-local PKN model is used to establish the fundamental decoupling between dynamics and kinematics, which leads to the emergence of a similarity solution – termed the sunset solution – close to the time of collapse of the fracture. The multiscale PKN numerical solutions agree well with those for a fully planar multiscale rectangular hydraulic fracture model in a three-dimensional elastic medium. The scaling laws and the emergence of

the sunset solution are confirmed by the PKN numerical model. The sunset solution also emerges in the fully planar numerical model and persists beyond the collapse time of the PKN model, by which time its footprints have separated from the upper and lower constraining sedimentary layer boundaries and have assumed self-similar elliptic shapes that shrink as they approach collapse.

**Key words:** lubrication theory, boundary layer structure, boundary integral methods

## 1. Introduction

Hydraulic fractures (HFs) are a class of fractures driven to propagate in a brittle solid medium by the injection of a viscous fluid. Hydraulic fractures occur naturally when: magma driven by buoyancy forces forms dykes and sills, see (Lister 1990; Roper & Lister 2007) for example; gravity and buoyancy-driven fluid flow within crevasses leads to ice calving events on ice shelves (Zarrinderakht *et al.* 2022, 2024); turbulent flow drives crack-like growth of subglacial lakes (Tsai & Rice 2010); and fluid driven cracks also lead to the failure of dams (Penman 1977; Bolzon & Cochetti 2003). Hydraulic fractures are also deliberately engineered in a variety of applications, including: the enhanced extraction of hydrocarbons (Economides & Nolte 2000); cave inducement in mining operations (van As & Jeffrey 2000); the measurement of the leak-off coefficient of the rock (Nolte 1979) and the *in situ* geological stresses (Haimson 1989); the enhanced recovery of geothermal energy; and, more recently, for the generation of lens-shaped fractures for the geomechanical storage of energy (Bunger *et al.* 2023).

For the last five decades there has been considerable effort dedicated to the modelling of propagating HFs while fluid is still being injected, however, until very recently, there has been very little research into the post-injection dynamics of HFs. There is, however, considerable importance in gaining a fundamental understanding of the post-shut-in dynamics in order to be able to obtain more rigorous ways to estimate the leak-off coefficient (Nolte 1979) and *in situ* stress (Haimson 1989; Hayashi & Haimson 1991; Lakirouhani *et al.* 2016). By shut-in we imply that injection is halted and the inlet conduit is capped. In contrast to the assumption, commonly made in these post-injection analyses, that the fracture footprint remains fixed at its maximal extent, recent research has demonstrated that the post-shut-in dynamics is much more complex. Indeed, regarding post-shut-in arrest, Mori & Lecampion (2021) demonstrated that the fracture may in fact continue to propagate after shut-in until it ultimately arrests at an expanded footprint or it may, as assumed, arrest almost immediately after shut-in, depending on the mode of propagation (storage or leak-off) at the time injection ceases. The post-arrest deflation dynamics is even richer (see Peirce & Detournay (2022*b*)), exhibiting a waiting period during which the fracture deflates *in situ* while the stress intensity factor decays to zero, at which instant there is an exchange of asymptotic behaviour of the fracture aperture  $w$  with distance  $x$  from the tip from the linear elastic fracture mechanics asymptote  $w \sim x^{1/2}$  to a novel linear asymptote  $w \sim x$  associated with recession, while both asymptotes share a common intermediate asymptote  $w \sim x^{3/4}$ . Moreover, close to the point of collapse of the fracture there is a fundamental decoupling of dynamics from kinematics, which gives rise to a similarity solution known as the sunset solution (Peirce & Detournay 2022*a*). This analytic work has thus far been restricted to plane strain and radially symmetric fractures (Peirce 2022; Peirce & Detournay 2022*a,c*). Another application of receding fracture

solutions based on rigorous tip asymptotes has been to calibrate traditional numerical models of HF recession, which make use of a minimum aperture constraint (Talebkeikhah *et al.* 2025).

Subsequent to this calibration of the minimum width constraint approach, there has been a recent focus on HF driven to recede by fluid leak-off in more complex environments – beyond the simplifying assumptions such as radial symmetry. These include fractures, in which symmetry is broken by jump discontinuities in the *in situ* stress field, the elastic moduli, the toughness and/or the leak-off coefficient across sedimentary layers leading to large topological changes in the fracture footprint (Talebkeikhah *et al.* 2025). Moreover, as an extension to the recession models involving closure to a constant minimum aperture constraint, there has recently been a study on recession in the context of closure on leaking proppant (Peirce *et al.* 2024, 2025). One of the conclusions of these studies has been that the emergence of the sunset solution close to collapse is more ubiquitous than the quite restrictive simplifying assumptions required to establish its origin and existence analytically. Much of this symmetry breaking is induced by the sedimentary layers through which the HF needs to pass during their evolution. Despite the significant symmetry-breaking induced by the layering, it frequently occurs that, close to the point of collapse, the fracture recession within the injection layer ultimately reverts to a receding rectangular fracture. A rectangular fracture contained between two sedimentary layers (see figure 1) is precisely the geometry that leads to the so-called PKN model (Perkins & Kern 1961; Nordgren 1972). Nolte (1991) and Sarvaramini & Garagash (2015) have introduced a toughness correction to the PKN model in the form of a pressure boundary condition applied at the fracture tip. Since the development of the non-local formulation of the PKN model (Adachi & Peirce 2008), it has been possible to incorporate more physical effects such as the effect of the fracture toughness rigorously (Dontsov & Peirce 2015a, 2016). However, surprisingly, to our knowledge, a rigorous analysis of the multiscale tip asymptotes for propagating PKN fractures has not been developed.

Given that it is amenable to analysis and the importance of the PKN geometry as a model for contained HF as well as the limiting shape of fractures in layered materials that have had more complex footprints, this paper explores the recession of PKN fractures. Tip vertex and multiscale asymptotes have proven extremely useful in the development of efficient and accurate numerical algorithms able to capture all the multiscale behaviour typically encountered during the evolution of a HF on a relatively coarse mesh (Peirce & Detournay 2008; Lecampion *et al.* 2013; Peirce 2015, 2016; Dontsov & Peirce 2017). To establish the required asymptotes for PKN fractures, in this paper we perform a detailed study of the multiscale PKN tip asymptotes for propagating fractures, the PKN tip and intermediate asymptotes to capture deflation due to leak-off while the fracture remains arrested, and the PKN tip and intermediate asymptotes for the transition to the recession asymptote. We establish a simple identification procedure that eliminates the necessity for a complete re-analysis for the PKN case, as it renders the governing equations for the semi-infinite PKN and plane strain equations formally identical. Using this transformation procedure, it is trivial to establish the PKN vertex asymptotes from the corresponding plane strain asymptotes. For these vertex asymptotes the pre-factors of the PKN asymptotes may differ from those of the equivalent plane strain asymptotes, but the power laws are all the same. However, the real benefit of this transformation procedure is in the determination of the edge and multiscale asymptotes as the capacity to transform the plane strain asymptotes to the corresponding PKN asymptotes makes it possible to deploy the same code segments that were developed for implementing the plane strain asymptotes directly for the PKN case.

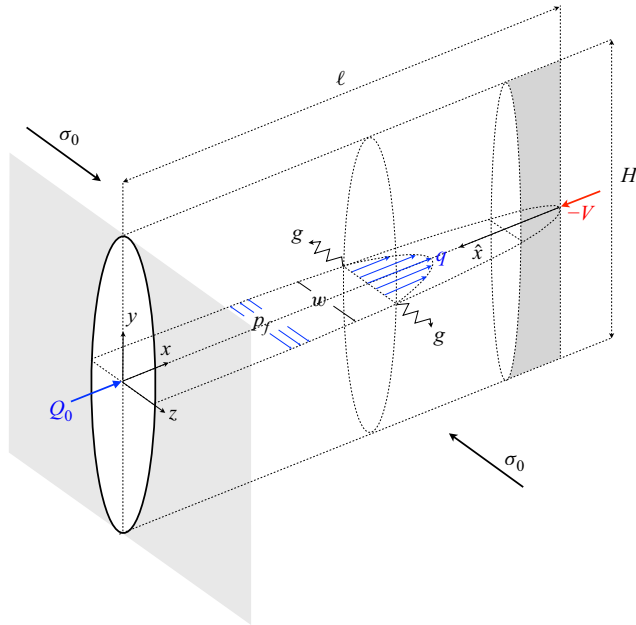


Figure 1. Schematic showing the PKN fracture geometry along with the coordinate systems used in the model. Within the rectangular fracture, fluid is being transported with a flux  $q$  while the leading edge is moving with a velocity  $V$ , and fluid is being lost to the porous rock at a velocity  $g$ .

In order to investigate the emergence of the sunset solution as a characteristic of the PKN model equations close to the point of collapse, we make use of the asymptotic analysis of the non-local PKN elasticity operator performed in Adachi & Peirce (2008), which established the near-field and far-field behaviour for points within and remote from the tip region. Other than the inner near-to-tip and outer remote-from-tip decomposition required for the analysis of the PKN fracture, the methodology is very similar to that of the plane strain and radial cases considered in Peirce & Detournay (2022a).

In § 2, we present the governing equations for the model of a planar rectangular fracture in a three-dimensional (3-D) elastic medium and its relation to the non-local PKN model; in § 3, we perform an asymptotic analysis of the non-local elasticity operator for the PKN model and determine the vertex and multiscale asymptotes associated with a propagating, deflating while arrested, and receding PKN fracture; in § 4, we test these asymptotes by comparing the numerical solutions of the rectangular planar 3-D fracture model with the corresponding numerical solutions of the PKN model, which is endowed with all the propagation, arrest, and recession asymptotes; in § 5, we use a scaling analysis to determine the characteristic power laws for arrest, which are verified by performing a parametric sweep using the PKN numerical solution; in § 6, we present the analysis to establish the emergence of the sunset similarity solution for receding PKN fractures as they approach the time of collapse  $t_c$ .

## 2. Mathematical model

The mathematical model describing the dynamics of a fluid driven fracture needs to account for the dominant physical processes involved, namely: the deformation of the rock due to the fracture opening; a mechanism for fracture growth; a description of the fluid flow within the fracture; and the leak-off of fluid to the surrounding porous medium.

In order that the model is tractable we make the following simplifying assumptions: the fracture propagates in a linear elastic solid characterised by the Young's modulus  $E$  and Poisson's ratio  $\nu$ ; growth of the fracture is assumed to be mode I according to linear elastic fracture mechanics (LEFM) and is modulated by fracture toughness  $K_{Ic}$ ; fluid flow within the fracture is assumed to be laminar, follows lubrication theory, and the fluid is assumed to be incompressible and Newtonian with a dynamic viscosity  $\mu$ ; we restrict ourselves to leak-off of fluid that is governed by Carter's model (Carter 1957) characterised by the leak-off coefficient  $C_L$ ; we assume that the fluid and fracture fronts coalesce; and the solid medium is assumed to be homogeneous so that  $E$ ,  $\nu$ ,  $K_{Ic}$  and  $C_L$  are all constant.

The fracture plane is assumed to develop along the path of least resistance, which is typically normal to the minimum principal component  $\sigma_0$  of the far-field compressive stress tensor. The above assumption that the fluid and fracture fronts coalesce, is based on the result, established by Garagash & Detournay (2000), that when subjected to large far-field stress conditions, the lag between the fracture front and the fluid front becomes negligible. As a result of large jump discontinuities in  $K_{Ic}$  and/or  $\sigma_0$  across the interfaces between sedimentary layers, it is possible for a HF to be contained within a rectangular subregion of the fracture plane. In this paper, we consider situations in which such jump discontinuities have restricted growth of the fracture to a horizontal channel within the fracture plane between two sedimentary layers, see figure 1. The Carter (1957) model assumes fluid leak-off is independent of the pressure and proportional to the inverse square root of the elapsed time since first exposure of the rock to the fracturing fluid at a given point. This inverse square root relationship represents a lumped model (see Adachi 2001) combining two fluid leak-off processes – both of which involve an inverse square root of the time lag: one captures the build-up of a filter cake by particle deposition on the walls of the fracture and the other represents the 1-D diffusion of fluid into the porous reservoir. The pre-factors for both of these component processes depend on  $\Delta p = p_f - p_0$ , where  $p_f$  is the fluid pressure within the fracture and  $p_0$  is the pore pressure within the reservoir. The justification for the assumption that this pre-factor is independent of pressure is as follows: we assume that the net pressure  $p_f - \sigma_0$ , which drives the fracture to propagate, is small compared with  $\sigma_0 - p_0$ . Thus  $p_f - p_0 = (p_f - \sigma_0) + (\sigma_0 - p_0) \approx \sigma_0 - p_0$ , which is constant so that the almost constant pre-factor is referred to as the leak-off coefficient  $C_L$ . The study of pressure-dependent leak-off is an active area of recent research (Kanin Garagash & Osipov 2020; Kanin *et al.* 2020) and beyond the scope of this paper.

## 2.1. Governing equations for a PKN hydraulic fracture in a permeable medium

Since the solid medium is assumed to be homogeneous, the fracture will grow symmetrically about the injection point. We choose to locate the origin of the  $x, y$  coordinate system at this point (see figure 1). The primary unknowns in a HF problem are the field variables comprising the fracture aperture  $w(x, y, t)$ :  $z = \pm w(x, y, t)/2$  and the fluid pressure  $p_f(x, y, t)$  within the fracture (or the net pressure  $p(x, y, t) = p_f(x, t) - \sigma_0$ ), both functions of  $x, y$  and  $t$ , and the fracture half-length  $\ell(t)$ , which, along with the constant fracture height  $H$ , define the evolving fracture geometry  $\mathcal{F}(t) = [-\ell(t), \ell(t)] \times [-H/2, H/2]$ . The solution depends on the volumetric injection rate  $Q(t)$  and four alternate material parameters defined in order to keep subsequent formulae uncluttered, namely: the plane strain modulus  $E'$ , the alternate viscosity  $\mu'$ , the alternate fracture toughness  $K'$ , and alternate Carter leak-off coefficient  $C'$ , which are defined as follows:

$$E' = \frac{E}{1 - \nu^2}, \quad \mu' = 12\mu, \quad K' = \left(\frac{32}{\pi}\right)^{1/2} K_{Ic}, \quad C' = 2C_L. \quad (2.1)$$

## 2.1.1. Elasticity

The equations relating the aperture  $w$  to the net pressure  $p$  on the walls of a planar fracture occupying the rectangular region  $(x, y) \in [-\ell, \ell] \times [-H/2, H/2]$  in an infinite, homogeneous, elastic solid can be condensed into a hypersingular integral equation of the form (see [Appendix A.2](#) and Crouch & Starfield 1983; Hills *et al.* 1996)

$$p(x, y, t) = -\frac{E'}{8\pi} \int_{-\ell}^{\ell} \int_{-H/2}^{H/2} \frac{w(x', y', t) dx' dy'}{[(x' - x)^2 + (y' - y)^2]^{3/2}}. \quad (2.2)$$

If the aspect ratio of the rectangular fracture is large, i.e.  $\ell \gg H$ , the typical assumption that is made in the PKN approximation (Perkins & Kern 1961; Nordgren 1972) is that a state of plane strain prevails for vertical cross-sections. In a state of plane strain  $w$  is independent of  $x'$  and (2.2), in the limit  $\ell \rightarrow \infty$ , is reduced (see A.3.1 of [Appendix A](#)) to that of a plane strain fracture in the vertical direction with semi-height  $H/2$ . Now, under the assumption that the pressure in such vertical cross-sections is constant, (Adachi & Peirce 2008) used the elliptic shape of the Sneddon solution for a plane strain fracture subject to a constant pressure (Sneddon 1995) (see also A.4) to motivate the following ansatz for the fracture aperture  $w(x, y, t)$  in which the  $x$  and  $y$  variables are assumed to be separated into the following product:

$$w(x, y, t) = w(x, 0, t) \sqrt{1 - (2y/H)^2}. \quad (2.3)$$

Now applying the vertical averaging operator  $\mathcal{A}(\cdot) := \frac{1}{H} \int_{-H/2}^{H/2} dy$  to (2.3) and defining  $\bar{w} := \mathcal{A}(w)$  we obtain

$$w(x, 0, t) = \frac{4}{\pi} \bar{w}(x, t). \quad (2.4)$$

Substituting the ansatz (2.3) into (2.2) and evaluating the inner iterated integral explicitly, makes it possible to reduce the planar integral equation to a 1-D integral equation (Adachi & Peirce 2008) as follows:

$$p(x, t) = -\frac{E'}{2\pi^2} \int_{-\ell}^{\ell} \bar{w}(x', t) \left[ \int_{-H/2}^{H/2} \frac{\sqrt{1 - (2y'/H)^2} dy'}{[(x' - x)^2 + y'^2]^{3/2}} \right] dx', \quad (2.5)$$

$$= \frac{\bar{E}}{\pi H} \int_{-\ell}^{\ell} \bar{w}(x', t) \frac{dG(2(x' - x)/H)}{dx'} dx', \quad (2.6)$$

where

$$\bar{E} = (2/\pi)E', \quad G(s) = \frac{\sqrt{1+s^2}}{s} E\left(\frac{1}{1+s^2}\right) \quad (2.7)$$

and

$$E(m) = \int_0^{\pi/2} \sqrt{1 - m \sin^2 \theta} d\theta \quad (2.8)$$

is the complete elliptic integral of the second kind. This non-local approximation to the PKN geometry has also been extended (Dontsov & Peirce 2015a) to include slender geometries such as the so-called P3D geometry (Adachi *et al.* 2010). We observe that



the kernel  $G$  of the integral equation (2.6) has the following asymptotic behaviour (Adachi & Peirce 2008):

$$G(\rho) \stackrel{\rho \rightarrow 0}{\sim} \left( \frac{1}{\rho} - \frac{1}{2} \rho \ln \rho + O(\rho) \right), \quad G(\rho) \stackrel{\rho \gg 1}{\sim} \frac{\pi}{2} \left( \text{sign}(\rho) + \frac{1}{4\rho^2} + O(\rho^{-4}) \right) \quad \text{and} \\ G'(\rho) \stackrel{\rho \gg 1}{\sim} \pi \delta(\rho). \quad (2.9)$$

Using the scaling property of the delta function  $\delta(cs) = (\delta(s)/|c|)$  and the asymptotic behaviour (2.9)<sub>c</sub>, we observe that, for points  $|x - \ell| \gg H/2$  away from the tip region, which we define as  $|x - \ell| < H/2$ , the non-local elasticity equation (2.6) reduces to the classic local pressure-width equation

$$p = \bar{E} \frac{\bar{w}}{H}. \quad (2.10)$$

We will revisit this formal calculation in § 3.2.2, in which we consider the asymptotic behaviour of the pressure within and away from the tip region.

### 2.1.2. Lubrication

The Reynolds lubrication equation is obtained by combining Poiseuille's law and the continuity equation to yield

$$\frac{\partial w}{\partial t} = \frac{1}{\mu'} \nabla \cdot (w^3 \nabla p) - g(x, y, t) + Q(t) \delta(x, y). \quad (2.11)$$

We assume that the velocity of fluid leak-off to the porous medium  $g(x, y, t)$  is captured by Carter's leak-off model  $g(x, y, t) = (C'/\sqrt{t - t_0(x, y)})$ , where  $t_0(x, y)$  denotes the time of first exposure of point  $(x, y)$  to the fracturing fluid (Carter 1957). The point source is represented by the  $\delta$ -function in (2.11) and we will be considering a propagation phase during which the fluid is injected at a constant volumetric rate  $Q_0$  followed by a shut-in phase initiated at time  $t_s$ , after which time there is no further fluid injected into the fracture. Thus the source function  $Q(t)$  can be expressed as

$$Q(t) = \begin{cases} Q_0 & 0 < t < t_s \\ 0 & t \geq t_s. \end{cases} \quad (2.12)$$

Applying the vertical averaging operator  $\mathcal{A}(\cdot)$  to (2.11) we obtain

$$\frac{\partial \bar{w}}{\partial t} = \frac{1}{\bar{\mu}} \frac{\partial}{\partial x} \left( \bar{w}^3 \frac{\partial p}{\partial x} \right) - g(x, t) + Q(t) \frac{\delta(x)}{H}, \quad (2.13)$$

where  $\bar{\mu} = (\pi^2/12)\mu' = \pi^2\mu$  and  $g(x, t) = C'/(\sqrt{t - t_0(x)})$ . We note that, in contrast to (2.11), the  $\delta$ -function here implicitly represents a uniformly distributed line source over the full height of the channel, i.e. covering the interval  $y \in [-H/2, H/2]$ , but with an area injection rate  $Q(t)/H$  scaled to be equivalent to the volumetric injection rate of the point source given in (2.11).

Combining the averaged lubrication equation (2.13) with the local elasticity equation (2.10), we obtain the classical porous medium partial differential equation (PDE) that governs the evolution of the PKN fracture (Kemp 1989; Kovalyshen & Detournay 2010)

$$\frac{\partial \bar{w}}{\partial t} = \frac{\bar{E}}{4\bar{\mu}H} \frac{\partial^2 \bar{w}^4}{\partial x^2} - g(x, t) + Q(t) \frac{\delta(x)}{H}. \quad (2.14)$$

### 2.1.3. Initial, boundary and propagation conditions at the moving front $\ell(t)$

Initial conditions: the initial conditions are formally given by

$$\ell = 0, \quad \bar{w} = 0, \quad p = 0, \quad \text{at } t = 0. \quad (2.15)$$

Boundary conditions: for coalescent fluid and fracture fronts the boundary conditions at the crack tips  $x = \pm\ell$  are given by zero fracture aperture and zero flux conditions (Detournay & Peirce 2014)

$$\bar{w} = 0, \quad \bar{w}^3 \frac{\partial p}{\partial x} = 0, \quad \text{at } x = \pm\ell. \quad (2.16)$$

For a symmetric fracture the  $\delta$ -function source can be replaced by an equivalent flux boundary condition at  $x = 0$

$$\frac{1}{\bar{\mu}} \bar{w}^3 \frac{\partial p}{\partial x}(0^+, t) = \frac{Q(t)}{2H}, \quad (2.17)$$

so that only half the fracture needs to be modelled.

Given these initial and boundary conditions, the lubrication equation, assuming Carter leak-off (2.13), can, after integrating both in time and space and exploiting symmetry, be expressed alternatively as the following global continuity equation:

$$2 \int_0^{\ell(t)} \bar{w}(x, t) dx + 4C' \int_0^{\ell(t)} \sqrt{t - t_o(x)} dx = V_f(t), \quad (2.18)$$

where

$$V_f = \begin{cases} Q_o t / H & 0 < t < t_s \\ V_o = Q_o t_s / H & t \geq t_s. \end{cases} \quad (2.19)$$

This equation simply establishes that the total volume of fluid injected at time  $t$  is equal to the volume of fluid contained in the crack plus the total volume of fluid lost to the permeable rock.

Propagation condition: since the fracture is assumed to propagate in limit equilibrium, LEFM (Rice 1968; Spence & Sharp 1985) implies that the alternate mode-I stress intensity factor  $K$  satisfies the following inequality constraint:

$$K := \bar{E} \lim_{x \rightarrow \pm\ell} \frac{\bar{w}(x)}{\sqrt{(\ell \mp x)}} \leq \bar{K}, \quad (2.20)$$

where  $\bar{K} = (8/\pi)^{1/2} K_{Ic}$ . Equality in (2.20) occurs when the fracture is propagating, i.e.  $V > 0$ , while strict inequality in (2.20) is associated with arrest characterised by  $V = 0$ ,  $0 \leq K < \bar{K}$ , and recession is characterised by  $V < 0$  and  $K = 0$ .

We note that in the PKN formulation we have introduced the barred quantities  $\bar{E}$ ,  $\bar{\mu}$ , and  $\bar{K}$  to keep the PKN equations uncluttered by numerical factors. For convenience, the alternate PKN parameters are summarised

$$\bar{E} = \frac{2}{\pi} E' = \frac{2}{\pi} \frac{E}{1 - \nu^2}, \quad \bar{\mu} = \frac{\pi^2}{12} \mu' = \pi^2 \mu, \quad \bar{K} = \left( \frac{8}{\pi} \right)^{1/2} K_{Ic}. \quad (2.21)$$

## 3. Asymptotic analysis

### 3.1. Stretched coordinate system

In the analysis that follows, it is convenient to introduce a stretched coordinate system  $s(t) = x/\ell(t)$ . The unknown functions in this coordinate system will be represented by



$\bar{w}(s, t)$  and  $p(s, t)$ . It is also convenient to introduce a coordinate  $\hat{x}$  located at the tip and pointing inwards toward the centre of the HF (see figure 1). The corresponding stretched coordinate located at the tip  $s = 1$  is represented by  $\hat{s} = 1 - s$  and the unknown functions in this case are  $\hat{w}(\hat{s}, t)$  and  $\hat{p}(\hat{s}, t)$ .

After integration by parts, the elasticity equation (2.6), in the tip-based stretched coordinate system  $\hat{s}$ , can be written in the form

$$\hat{p}(\hat{s}, t) = -\frac{\bar{E}}{\pi H} \int_0^2 \frac{d\hat{w}(\hat{s}', t)}{d\hat{s}'} G\left(\frac{\hat{s}' - \hat{s}}{\varepsilon}\right) d\hat{s}' = I_{\mathcal{A}} + I_{\mathcal{B}}, \quad (3.1)$$

where  $\varepsilon = H/(2\ell) \ll 1$ . For the purposes of the subsequent asymptotic analysis, it is convenient to decompose the domain of integration in (3.1) into the union of two disjoint subsets as follows:  $(0, 2) = \mathcal{A} \cup \mathcal{B}$ . The set  $\mathcal{A}$  is used to denote the set of points  $\hat{s}$  remote from the source point  $\hat{s}'$ , i.e.  $|\hat{s}' - \hat{s}| > \varepsilon$ , and the contribution from this region to the integral on the right of (3.1) is denoted by  $I_{\mathcal{A}}$ . The set  $\mathcal{B}$  is used to denote the set of points within an  $\varepsilon$ -neighbourhood of the source point, i.e.  $|\hat{s}' - \hat{s}| < \varepsilon$ , and the contribution from this region to the integral on the right of (3.1) is denoted by  $I_{\mathcal{B}}$ .

The lubrication equation (2.13) in the stretched tip coordinate system becomes

$$\frac{\partial \hat{w}}{\partial t} + (1 - \hat{s}) \frac{\dot{\ell}}{\ell} \frac{\partial \hat{w}}{\partial \hat{s}} = \frac{1}{\bar{\mu} \ell^2} \frac{\partial}{\partial \hat{s}} \left( \hat{w}^3 \frac{\partial \hat{p}}{\partial \hat{s}} \right) - \hat{g}(\hat{s}, t) + Q(t) \frac{\delta(\hat{s} - 1)}{H}, \quad (3.2)$$

where  $\hat{g}(\hat{s}, t) = C'/(\sqrt{t - t_0(\ell(1 - \hat{s}))})$  and  $0 \leq \hat{s} \leq 1$ .

### 3.2. Asymptotic analysis of the elasticity operator

In this subsection we investigate the impact that the distinct far- and near-field asymptotic behaviours of the elasticity kernel  $G(s)$ , provided in (2.9), have on the action of the non-local integral operator when the receiving point  $\hat{s}$  is remote from as well as near to the tip region. Although the aperture and pressure are functions of both  $\hat{s}$  and  $t$ , for brevity, in this subsection we will suppress the explicit dependence on  $t$ .

#### 3.2.1. Asymptotic expansions for the elasticity operator

Assuming  $\mathcal{A} = \{\hat{s}' \in (0, 2) : |\hat{s}' - \hat{s}| > \varepsilon\}$  and  $\mathcal{B} = \{\hat{s}' \in (0, 2) : |\hat{s}' - \hat{s}| < \varepsilon\}$ , we decompose the crack region  $(0, 2) = \mathcal{A} \cup \mathcal{B}$  into the union of a set  $\mathcal{A}$  within which the far-field expansion (2.9)<sub>b</sub> holds

$$I_{\mathcal{A}} \sim -\frac{\bar{E}}{2H} \int_{\mathcal{A}} \frac{d\hat{w}(\hat{s}')}{d\hat{s}'} \left[ \text{sign}\left(\frac{\hat{s}' - \hat{s}}{\varepsilon}\right) + \frac{\varepsilon^2}{4(\hat{s}' - \hat{s})^2} + \dots \right] d\hat{s}', \quad (3.3)$$

and a set  $\mathcal{B}$  within which the near-field expansion (2.9)<sub>a</sub> holds

$$I_{\mathcal{B}} \sim -\frac{\bar{E}}{\pi H} \oint_{\mathcal{B}} \frac{d\hat{w}(\hat{s}')}{d\hat{s}'} \left[ \frac{\varepsilon}{\hat{s}' - \hat{s}} - \frac{1}{2} \frac{(\hat{s}' - \hat{s})}{\varepsilon} \ln \frac{|\hat{s}' - \hat{s}|}{\varepsilon} + \dots \right] d\hat{s}', \quad (3.4)$$

where the  $\oint$  symbol implies that the integral should be interpreted in a Cauchy principal value sense, which is necessary because of the Cauchy behaviour of the leading term in the asymptotic expansion of the kernel.

### 3.2.2. Outer expansion

To investigate the asymptotic behaviour of  $\hat{p}$  for receiving points  $\hat{s}$  away from the tip region, i.e.  $\hat{s} > \varepsilon$ , we choose  $\mathcal{A} = (0, \hat{s} - \varepsilon) \cup (\hat{s} + \varepsilon, 2)$  and  $\mathcal{B} = (\hat{s} - \varepsilon, \hat{s} + \varepsilon)$ . Integrating the first term in (3.3) directly and evaluating the subsequent terms in the expansion as in (Adachi & Peirce 2008), we obtain

$$\begin{aligned} I_{\mathcal{A}} &\sim \frac{\bar{E}}{H} \left\{ \frac{1}{2} [\hat{w}(\hat{s} - \varepsilon) + \hat{w}(\hat{s} + \varepsilon)] - \int_{\mathcal{A}} \frac{d\hat{w}(\hat{s}')}{d\hat{s}'} \left[ \frac{\varepsilon^2}{8(\hat{s}' - \hat{s})^2} + \dots \right] d\hat{s}' \right\} \\ &\sim \frac{\bar{E}}{H} \left\{ \hat{w}(\hat{s}) - \frac{1}{4} \varepsilon^2 \ln \varepsilon \frac{d^2 \hat{w}(\hat{s})}{d\hat{s}^2} + \dots \right\}, \end{aligned} \quad (3.5)$$

and the leading behaviour of (3.4) can be shown to be (Adachi & Peirce 2008)

$$I_{\mathcal{B}} \sim -\frac{\bar{E}}{\pi H} \left\{ \varepsilon^2 \left( \frac{41}{18} + \frac{2}{3} \ln 2 \right) \frac{d^2 \hat{w}(\hat{s})}{d\hat{s}^2} + \dots \right\}. \quad (3.6)$$

Combining these two asymptotic expansions we observe that the asymptotic expansion for the pressure at receiving points away from the tip region is dominated by the far-field behaviour within the set  $\mathcal{A}$  and is given by

$$\hat{p}(\hat{s}) = \frac{\bar{E}}{H} \left[ \hat{w}(\hat{s}) - \frac{1}{4} \varepsilon^2 \ln \varepsilon \frac{d^2 \hat{w}(\hat{s})}{d\hat{s}^2} + O(\varepsilon^2) \right]. \quad (3.7)$$

We note that the leading behaviour of this so-called outer expansion for the pressure is the same as that for the local elasticity operator (2.10), which was derived formally using the properties of the  $\delta$ -function.

### 3.2.3. Inner expansion

For receiving points  $\hat{s}$  within the tip region  $\hat{s} < \varepsilon$ , we choose  $\mathcal{A} = (\hat{s} + \varepsilon, 2)$  and  $\mathcal{B} = (0, \hat{s} + \varepsilon)$  and assume that  $\hat{w}(\hat{s}) = \hat{A}(t) \hat{s}^\lambda$ . From the analysis in (Adachi & Peirce 2008), it follows that the leading behaviour of  $I_{\mathcal{A}}$  is given by

$$I_{\mathcal{A}} \sim O(\varepsilon^2), \quad (3.8)$$

and, defining the transformation  $\hat{\xi} = \hat{s}/\varepsilon$  as in (Adachi & Peirce 2008), the expression for  $I_{\mathcal{B}}$  becomes

$$\begin{aligned} I_{\mathcal{B}} &\sim -\frac{\bar{E} \hat{A} \lambda \varepsilon^\lambda}{\pi H} \int_0^{1+\hat{\xi}} \hat{\xi}'^{(\lambda-1)} \left[ \frac{1}{\hat{\xi}' - \hat{\xi}} - \frac{1}{2} (\hat{\xi}' - \hat{\xi}) \ln |\hat{\xi}' - \hat{\xi}| + \dots \right] d\hat{\xi}' \\ &\sim -\frac{\bar{E} \hat{A} \lambda \varepsilon^\lambda}{\pi H} \left\{ \begin{array}{ll} -\pi \cot(\pi \lambda) \hat{\xi}^{\lambda-1} & \text{for } \frac{1}{2} \leq \lambda < 1 \\ -\ln |\hat{\xi}| & \text{for } \lambda = 1 \end{array} \right\} + C. \end{aligned} \quad (3.9)$$

Thus for receiving points within the tip region, the leading behaviour for the pressure corresponding to the aperture power law is of the form

$$\hat{p}(\hat{s}) \sim \frac{\bar{E} \hat{A}}{2\ell} \left\{ \begin{array}{ll} \lambda \cot(\pi \lambda) \hat{s}^{\lambda-1} & \text{for } \frac{1}{2} \leq \lambda < 1 \\ \frac{1}{\pi} \ln |\hat{s}| & \text{for } \lambda = 1 \end{array} \right\} + C. \quad (3.10)$$

We note that (3.10) is the PKN equivalent of the plane strain eigenfunction presented in appendix C of Spence & Sharp (1985) and derived in Appendix A (see (A35)).

### 3.3. Vertex asymptotes for the coupled equations

Throughout this section we will assume that the leading behaviour for the aperture is a power law  $\hat{w}(\hat{s}, t) \stackrel{\hat{s} \rightarrow 0}{\sim} \hat{A}(t)\hat{s}^\lambda$ . Substituting this aperture power law and the corresponding leading behaviour for the tip pressure (3.10) into the tip lubrication equation (3.2) leads to the following asymptotic relations:

$$\frac{1}{2} \leq \lambda < 1 : \dot{\hat{A}}\hat{s}^\lambda + \frac{\dot{\ell}}{\ell}\lambda\hat{A}\hat{s}^{\lambda-1} \sim \frac{\hat{A}^4\bar{E}}{\bar{\mu}\ell^3}\lambda(\lambda-1)(2\lambda-1)\cot(\pi\lambda)\hat{s}^{4\lambda-3} - \hat{g}, \quad (3.11)$$

$$\lambda = 1 : \dot{\hat{A}}\hat{s} + \frac{\dot{\ell}}{\ell}\hat{A} \sim \frac{\hat{A}^4\bar{E}}{\pi\bar{\mu}\ell^3}\hat{s} - \hat{g}. \quad (3.12)$$

We note that if  $\lambda > 1$  the aperture power law and the corresponding tip pressure cannot satisfy the lubrication equation and the elasticity equation simultaneously. The plain strain state plays a fundamental role in the tip asymptotics of any planar fracture with a smooth boundary in a 3-D elastic medium. Indeed, in the limit as the receiving point approaches the fracture boundary (see Peirce & Detournay (2008) and Appendix A.2), the planar elasticity integral equation (A27) reduces to that of a semi-infinite fracture in a state plane strain (A33). Comparing (3.10)<sub>a</sub> with (A35), we observe that the non-local PKN asymptote (3.10)<sub>a</sub> can be made formally identical to the plane strain asymptote (A35), by replacing  $\bar{E}$  in (3.10) by  $E'/2$ . Moreover, if we replace  $\bar{\mu}$  in the PKN lubrication equation (2.13) by  $\mu'$  then we obtain the plane strain lubrication equation – but for the difference in the source term, which is of no consequence in this asymptotic analysis. Thus by making the substitutions

$$\bar{E} \rightarrow \frac{E'}{2} \quad \text{and} \quad \bar{\mu} \rightarrow \mu', \quad (3.13)$$

the non-local PKN asymptotic relations (3.11)–(3.12) become precisely those for a HF in a state of plane strain (see for example (Peirce & Detournay 2022c)). Conversely, to transition from the plane strain asymptotic relations to those of the non-local PKN model, the following substitutions are required:

$$E' \rightarrow 2\bar{E} \quad \text{and} \quad \mu' \rightarrow \bar{\mu}. \quad (3.14)$$

The ability to transition from the plane strain asymptotic relations to those of the non-local PKN fracture, makes it possible to use the established plane strain propagation asymptotes (Detournay 2004, Dontsov & Peirce, 2015b; Detournay 2016) to determine the corresponding PKN asymptotes by making the substitutions (3.14). Not only do these substitutions make it possible to obtain the so-called vertex asymptotes for the PKN from those for plane strain, but they can also be used to determine the corresponding PKN edge and tri-process multiscale asymptotes. Indeed, the multiscale asymptotes (Garagash *et al.* 2011; Dontsov & Peirce 2015b), established for the plane strain case, can be used directly to obtain the PKN asymptotes by making use of the substitutions (3.14).

#### 3.3.1. Propagation asymptotes ( $K = \bar{K}$ , $V > 0$ )

Viscous asymptote: in the absence of leak-off and in an elastic medium with close to zero toughness, the dominant balance occurs between the second and third terms in (3.11). Matching these terms, we find  $\lambda = 2/3$  and, solving for  $\hat{A}$ , we obtain the viscous asymptote

$$\bar{w}_m(x) = \bar{\beta}_m \left( \frac{\bar{\mu} V}{\bar{E}} \right)^{1/3} (\ell - x)^{2/3}, \quad (3.15)$$

where  $\bar{\beta}_m = 3^{5/6}$ . Note that applying the substitutions (3.14) to the plane strain viscous asymptote  $w_m(x) = \beta_m (\mu' V / E')^{1/3} (\ell - x)^{2/3}$ , where  $\beta_m = 2^{1/3} 3^{5/6}$  (see Spence & Sharp 1985; Desroches *et al.* 1994), we recover (3.15).

Now if we combine the expression for the average width  $\bar{w}$  defined in (2.4) with the viscous asymptote  $w_m$ , we find that  $\bar{w} = (\pi/4) w_m = (3/4)^{1/3} \bar{w}_m(x)$ , which amounts to a 9 % difference between these two estimates for the average asymptote  $\bar{w}$ . This is not surprising considering the exchange of limits implied by that taking the asymptotic limit of the averaged equations to obtain  $\bar{w}_m$ , compared with the latter evaluation of  $\bar{w}$  by applying the averaging factor  $(\pi/4)$  to the plane strain viscous asymptote.

Leak-off asymptote: if leak-off is dominant, we replace  $\hat{g}$  by the asymptotic behaviour in the tip region  $\hat{g} \sim (C' \ell^{1/2}) / \ell^{1/2} \hat{s}^{1/2}$ , and find that the dominant balance is between the third and last terms in (3.11). It follows that  $\lambda = 5/8$  and, solving for  $\hat{A}$ , we obtain

$$\bar{w}_{\tilde{m}}(x) = \beta_{\tilde{m}} \left( \frac{\bar{\mu} C' V^{1/2}}{\bar{E}} \right)^{1/4} (\ell - x)^{5/8}, \quad (3.16)$$

where  $\beta_{\tilde{m}} = 4/[15(\sqrt{2} - 1)]^{1/4}$ . Note that if we apply the substitutions (3.14) to the classic Lenoach tip asymptote  $w_{\tilde{m}}(x) = \beta_{\tilde{m}} (2\mu' C' V^{1/2} / E')^{1/4} (\ell - x)^{5/8}$  see (Lenoach 1995), we obtain (3.16). If we combine the expression for the average width  $\bar{w}$  defined in (2.4) and the Lenoach tip asymptote  $w_{\tilde{m}}$ , we find that  $\bar{w} = (\pi/4) w_{\tilde{m}} = (3\pi/8)^{1/4} \bar{w}_{\tilde{m}}(x)$ , which amounts to a 4 % difference between these two estimates for the average asymptote  $\bar{w}$ .

Toughness asymptote: the toughness asymptote follows from the propagation condition (2.20)

$$\bar{w}_{\bar{k}}(x) = \frac{\bar{K}}{\bar{E}} (\ell - x)^{1/2}. \quad (3.17)$$

Note that if we apply the substitutions (3.14) to the plane strain tip asymptote  $w_{k'}(x) = (K' / E') (\ell - x)^{1/2}$ , we obtain (3.17). Alternatively, if we combine the expression for the average width  $\bar{w}$  defined in (2.4) and the plane strain tip asymptote  $w_{k'}(x)$ , we recover the toughness asymptote (3.17), i.e.  $\bar{w} = (\pi/4) w_{k'}(x) = \bar{w}_{\bar{k}}(x)$ .

### 3.3.2. Arrest asymptotes ( $0 \leq K < \bar{K}$ , $V = 0$ )

The arrest phase is characterised by  $V = 0$  while the stress intensity factor  $K$  steadily decreases from  $\bar{K}$  to 0 as fluid continues to leak from the fracture into the porous medium. During propagation  $\hat{g}$  is singular, however, after the fracture has come to rest  $\hat{g}$  is no longer singular, and, in fact, becomes more spatially uniform in the tip region as time progresses. In this case, it is appropriate to assume that  $\hat{g}(\hat{s}, t) \sim \hat{g}_0(t)$ .

Arrest- $k$ -asymptote ( $K > 0$ ,  $V = 0$ ): during arrest ( $V = 0$ ) so the near-tip asymptote is thus given by LEFM

$$\bar{w}_k = \frac{K}{\bar{E}} (\ell - x)^{1/2}, \quad (3.18)$$

where  $K$  is a decreasing function of time. We refer to  $\bar{w}_k$  as the  $k$ -asymptote.

Arrest-recession transition- $g$ -asymptote ( $K = 0$ ,  $V = 0$ ): at the end of the arrest phase, both  $K$  and  $V$  vanish. Although the passage from arrest to recession is ephemeral, the transition is accompanied by a switch in the near-field asymptote. To construct the intermediate asymptote that applies at this transition point, we proceed as above and

assume a power law for the aperture, replace  $\hat{g}(\hat{s}, t)$  in (3.11) by  $\hat{g}_0(t)$ , and match the third and fourth terms in (3.11) to find  $\lambda = (3/4)$  and, solving for  $\hat{A}$ , we obtain

$$\bar{w}_g = \beta_{\bar{g}} \left( \frac{\bar{\mu} \hat{g}_0}{\bar{E}} \right)^{1/4} (\ell - x)^{3/4}, \quad (3.19)$$

where  $\beta_{\bar{g}} = (32/3)^{1/4} \simeq 1.807$  and we refer to  $\bar{w}_g$  as the  $\bar{g}$ -asymptote. We note that making the substitutions (3.14) for the  $g$ -asymptote derived in (Peirce & Detournay 2022b) we recover (3.19).

### 3.3.3. The recession asymptote- $r$ -asymptote ( $K = 0$ , $V < 0$ )

If  $V < 0$ , the  $g$ -asymptote  $\lambda = 3/4$  is no longer admissible as the second term in (3.11) would become infinite and violate the dominant balance. Thus the only possibility is that  $\lambda = 1$ , and matching the second and fourth terms in (3.12), we obtain the  $r$ -asymptote

$$\bar{w} = -\hat{g}_0(t) \frac{\ell}{\bar{E}} \hat{s} \quad \text{or} \quad \bar{w}_r(x) = \hat{g}_0(t) \frac{(\ell - x)}{|V|}. \quad (3.20)$$

We observe that the first and third terms in (3.12) match at the next order.

## 3.4. The connection problem to establish multiscale solutions

Vertex and multiscale tip asymptotic solutions (Garagash *et al.* 2011; Dontsov & Peirce 2015b; Detournay 2016) have proven to be extremely useful in the development of numerical algorithms to model propagating fractures (Adachi & Detournay 2008; Peirce & Detournay 2008; Lecampion *et al.* 2012; Peirce 2015, 2016; Dontsov & Peirce 2017), and, more recently, for the development of models for receding HF in which fluid loss to the porous elastic medium causes the fracture to deflate and close (Peirce 2022; Peirce & Detournay 2022b,c). These algorithms can achieve solutions with a high degree of precision, able to account for the vertex and multiscale behaviour at the finest length scale, while using a relatively coarse mesh. The fundamental idea for propagating and receding HF alike (Peirce & Detournay 2008; Peirce 2015; Dontsov & Peirce 2017; Peirce 2022; Peirce & Detournay 2022c) is to use a trial value for the fracture aperture  $\hat{w}$ , sampled at computational points within and adjacent to the fracture front, along with the applicable tip asymptote to estimate the fracture front location (or equivalently the local front velocity) at the current step. The front position for propagating or receding fractures is then adjusted iteratively and the aperture updated until both are consistent with the applicable asymptote. The efficacy of this approach was clearly demonstrated in a collaborative study that evaluated a number of numerical algorithms (Lecampion *et al.* 2012) and benchmarked their relative accuracy against an analytic solution and compared their relative efficiency.

The non-singular approach introduced in (Dontsov & Peirce 2015b) provides an effective way to determine these multiscale asymptotes, namely: the viscous-toughness-leak-off multi-scale asymptotes for propagating fractures. (Peirce & Detournay 2022b) used the non-singular approach to determine the  $k-g$  edge solution to capture the deflation of an arrested HF while the stress intensity factor decays to zero and the  $r-g$  edge solution to capture the acceleration of the receding fracture from the arrested state  $\dot{\ell} = 0$  till the  $r$ -asymptote fully occupies the tip region.

The starting point for the non-singular approach (Dontsov & Peirce 2015b) is the governing integral equation over the tip region that relates the fluid pressure to the fracture aperture. For the PKN fracture this integral equation is obtained by integrating (2.6) by

parts, transforming to the tip coordinate  $\hat{x}$ , zooming into the tip region, and making use of the leading-order expansion for  $G$ , to yield

$$p(\hat{x}, t) \sim -\frac{\bar{E}}{2\pi} \int_0^\infty \frac{d\bar{w}(\hat{x}')}{d\hat{x}'} \frac{d\hat{x}'}{\hat{x}' - \hat{x}}. \quad (3.21)$$

The corresponding lubrication equation for the PKN fracture that expresses fluid conservation in the tip region is

$$\frac{\bar{w}^3}{\bar{\mu}} \frac{dp}{d\hat{x}} = V\bar{w} + \int_0^{\hat{x}} \hat{g}(\hat{s}) d\hat{s}, \quad (3.22)$$

where the boundary conditions (2.16) have been used and

$$\hat{g}(\hat{x}) = \begin{cases} \frac{C'V^{1/2}}{\hat{x}^{1/2}} & \text{for } V > 0 \\ \hat{g}_0 & \text{for } V \leq 0. \end{cases} \quad (3.23)$$

We observe that the substitution (3.13) reduces (3.21) to the plane strain equation (A33) derived in Appendix A, while (3.22) is rendered formally identical to the corresponding lubrication equation for propagating and deflating fractures analysed in Dontsov & Peirce, (2015b) and Peirce & Detournay, (2022b), respectively. The consequence of this formal equivalence is profound as the plane strain multiscale asymptotes can be used directly provided the appropriate transformations are made.

#### 4. Comparison between PKN model with asymptotes and a fully planar 3-D model

Having established the multiscale vertex, edge, and tri-process asymptotes for a PKN fracture, in this section we provide numerical results comparing numerical solutions to the PKN model equations (2.6) and (2.13) subject to the initial (2.15) and boundary (2.16) conditions to the solutions to a planar fracture model in a 3-D elastic medium (PL3D) governed by (2.2) and (2.11) also subject to zero aperture and flux boundary conditions. The PKN equations are solved using an implicit moving mesh algorithm (IMMA), similar to that described in Dontsov & Peirce (2015a) and Dontsov (2016), in which all the multiscale tip asymptotes for propagation, arrest and recession, described in §3, are used to determine the location of the moving front. The planar 3-D equations are solved using the implicit level set algorithm (ILSA) (Peirce & Detournay 2008; Peirce 2015; Dontsov & Peirce 2017; Zia & Lecampion 2020), which uses the viscous-toughness-leak-off multiscale asymptotes (Dontsov & Peirce 2015b, 2017) to model fracture propagation, while recession of the fracture boundary is captured using a minimum width constraint (Zia & Lecampion 2020; Talebkeikhah *et al.* 2025) for points at which the fracture was previously open but ultimately close due to fluid leak-off. We will refer to the former procedure as the IMMA-PKN algorithm and the latter as the ILSA-PL3D algorithm. We provide two numerical examples, the first example compares the IMMA-PKN and the ILSA-PL3D results for a parameter set that one might expect in the field. This example focusses on the pre- and post-shut-in propagation up till the time of arrest and enables us to compare the IMMA-PKN and ILSA-PL3D algorithms when their respective viscous-toughness-leak-off multiscale propagation asymptotes are used. For this example a specialised version of the ILSA-PL3D code was used in which the fracture boundary was not permitted to propagate beyond the channel  $|y| < H/2$ . The second example enables

us to compare the IMMA-PKN and ILSA-PL3D solutions for propagation pre- and post-shut-in, arrest and deflation during arrest, and recession. The IMMA-PKN model uses the PKN viscous-toughness-leak-off multiscale propagation asymptotes up to the point of arrest, the  $k-g$  and  $r-g$  edge solutions to model the transition from arrest to recession as well the  $r-$  asymptote to capture recession. The ILSA-PL3D algorithm uses the viscous-toughness-leak-off multiscale asymptote for propagation and a width constraint to model the HF closing on itself and the recession of the free boundary. In this model, the fracture was restricted to evolve within the channel  $|y| < H/2$  by a tenfold increase in the fracture toughness between the channel and the region  $|y| > H/2$ . A study has been conducted (Talebkeikhah *et al.* 2025) to calibrate the minimum width constraint used by the ILSA-PL3D algorithm against a radial solution (Peirce 2022), which uses an IMMA scheme endowed with the viscous-toughness-leak-off, arrest, and recession asymptotes. A width constraint strategy, shown to yield accurate results in that study, was used in this comparison.

#### 4.1. Propagation, shut-in and arrest

We consider a HF that propagates under the continuous injection of a viscous fluid until the shut-in time  $t_s = 1500$  s, after which injection is discontinued and the injection conduit is capped. The field-like parameters are:  $E = 9.5$  GPa,  $\nu = 0.2$ ,  $\mu = 0.1$  Pa s,  $C = 8.2431 \times 10^{-6}$  ms $^{-1/2}$ ,  $K_{IC} = 1.0$  MPa m $^{1/2}$ ,  $Q_0 = 10^{-3}$  m $^3$  s $^{-1}$  and  $H = 20$  m.

This parameter set corresponds to the dimensionless shut-in time  $\omega \sim 2.0 \times 10^{-3}$  and arrest regime parameter  $\bar{\phi}^V \sim 2.49 \times 10^2$ . The dimensionless shut-in time is defined to be  $\omega = t_s / \bar{t}_{m\tilde{m}}$ , where  $t_s$  is the actual shut-in time and  $\bar{t}_{m\tilde{m}}$  is the time scale at which propagation transitions from being viscosity dominated to being dominated by leak-off. The arrest regime parameter is defined to be the ratio of two time scales  $\bar{\phi}^V = (\bar{t}_{mk}^V) / (\bar{t}_{m\tilde{m}}^V)$ , where  $\bar{t}_{mk}^V$  is the time (assuming a fixed injected volume, which is appropriate post shut-in) at which propagation transitions from viscosity to toughness dominated propagation, while  $\bar{t}_{m\tilde{m}}^V$  again represents the transition time between viscosity dominated and leak-off dominated propagation – but now assuming a fixed injected volume. The  $V$  superscript indicates fixed volume propagation.

If the time of arrest  $t_a \sim \bar{t}_{mk}^V \ll \bar{t}_{m\tilde{m}}^V$  then  $\phi^V \ll 1$ , and the fracture is propagating in the toughness regime at the time of arrest but still contains a significant amount of fluid that needs to leak-off before recession can start. Conversely, if  $t_a \sim \bar{t}_{m\tilde{m}}^V \ll \bar{t}_{mk}^V$  then  $\bar{\phi}^V \gg 1$ , and the fracture is propagating in the leak-off regime at the time of arrest and has lost sufficient fluid to preclude significant further propagation of the fracture. In this case recession will start almost immediately after a very short arrest period. See § 5 for more detail.

In the top plot in figure 2, we compare the first quadrant projections of the pre- and post-shut-in fracture footprints obtained using the ILSA-PL3D and IMMA-PKN algorithms. In the middle plot we compare the corresponding pre-shut-in fracture apertures, and in the bottom plot we compare the post-shut-in fracture apertures that correspond to the remaining fracture footprints shown in the top figure. As the fracture approaches arrest, the density of the footprints increases and the successive fracture apertures become much closer together. The PKN and PL3D solutions show very close agreement. The slight discrepancy for the first fracture footprint shown is to be expected as the initially radial planar fracture has just touched the upper boundary at which point the aspect ratio is close to unity so one would not expect the PKN solution to be particularly close to the PL3D solution.

In figure 3, we compare time evolution plots of the ILSA-PL3D (dashed red) and IMMA-PKN (solid black) solutions for the: aspect ratio  $2\ell/H$ , the fracture aperture at the injection



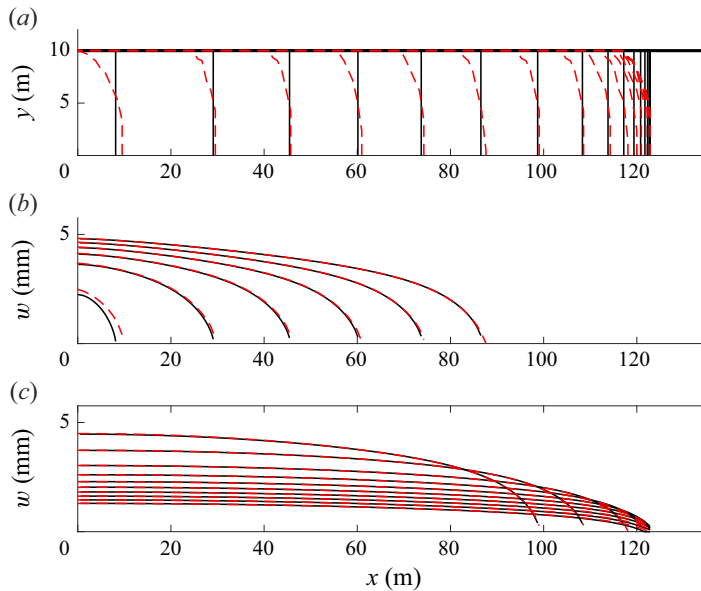


Figure 2. (a) The pre- and post-shut-in ILSA-PL3D fracture footprints (dashed red) and the corresponding IMMA-PKN fracture front positions (solid black), (b) the pre-shut-in fracture apertures that correspond to the fracture footprints in the top figure, (c) the post-shut-in fracture apertures that correspond to the fracture footprints in the top figure.

point, the fluid pressure at the injection point and the efficiency, which is defined to be

$$\eta = 2 \int_0^{\ell(t)} \bar{w}(x, t) dx / V_f, \quad (4.1)$$

The shut-in time is indicated on the aspect ratio plot by the solid black square ■, which corresponds to the points at which the curvatures in the other plots in this figure change abruptly. As was the case with the solutions provided in figure 2, the ILSA-PL3D and IMMA-PKN solutions show close agreement. The only noticeable discrepancy is in the fluid pressure at the injection point near the start of injection, which is again due to the transition from a radial fracture (for the ILSA-PL3D algorithm) to a rectangular fracture during the initial stages of growth of the fracture.

The close agreement between the two sets of results, even in this environment in which multiple physical processes compete to determine the evolution of the fracture boundary, demonstrates the utility of the PKN asymptotes established by the analysis in § 3. Having established the efficacy of the PKN asymptotes in determining the post-shut-in dynamics of the HF propagation and the clear identification of the time of arrest, the IMMA-PKN algorithm is used to confirm the scaling analysis performed in § 5.

#### 4.2. Propagation, shut-in, arrest and recession

We now provide IMMA-PKN and ILSA-PL3D solutions for a HF that evolves within a rectangular region of constant height  $H$  and growing length  $2\ell$ . In the case of the ILSA-PL3D algorithm the HF is constrained to propagate between two sedimentary layers by introducing a tenfold jump in the fracture toughness  $K_{Ic}$  across layer interfaces located at  $y = \pm H/2$ . Naturally, the rectangular footprint is a fundamental assumption of the PKN model. After shut-in, when the injection of fluid is discontinued, the fracture continues to propagate but gradually slows until it arrests when the stress intensity factor at the leading

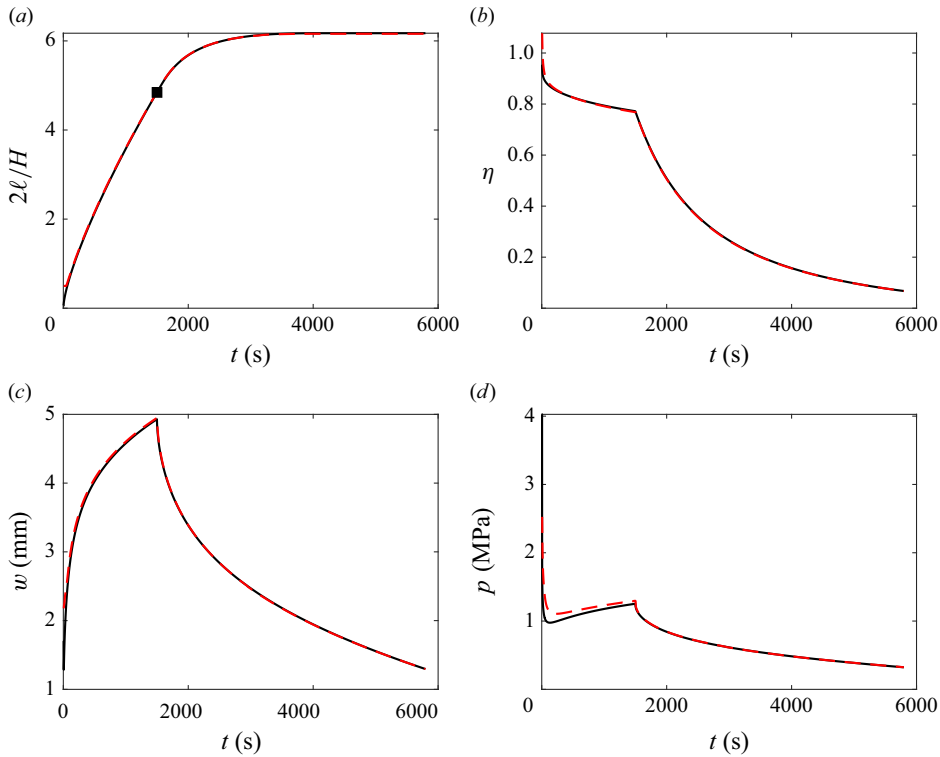


Figure 3. (a) the ILSA-PL3D (dashed red) and the IMMA-PKN (solid black) aspect ratios as a function of time, (b) the efficiencies  $\eta$  as functions of time, (c) the fracture apertures at the injection point as functions of time, (d) the fluid pressures at the injection point as functions of time.

front of the fracture drops below the fracture toughness. This deceleration is not only due to the spreading of the fracture as the pressure gradients reduce but also due to the leak-off of fluid to the porous elastic medium. After arrest, the fracture continues to deflate due to fluid leak-off until the stress intensity factor is reduced to zero. Thereafter, with further loss of fluid due to leak off to the porous medium, the fracture tip starts to recede as the open parts of the fracture resume contact. This recession process is modelled by the ILSA-PL3D algorithm by the introduction of a minimum width constraint upon closure, while the IMMA-PKN algorithm uses the recession asymptote.

Rather than a selection of a set of parameters that might be encountered in the field, the following parameter set was chosen in order to be able to accurately model the rectangular fracture evolution and recession process using the ILSA-PL3D algorithm:  $E = 0.0096$  GPa,  $\nu = 0.2$ ,  $\mu = 300$  Pa s,  $C = 1.9758 \times 10^{-3}$  ms $^{-1/2}$ ,  $K_{IC} = 0.01$  MPa m $^{1/2}$ ,  $t_s = 10^8$  s,  $Q_0 = 1$  m $^3$ s $^{-1}$  and  $H = 216.8614$  m. This choice of elastic moduli and fracture height  $H$  leads to large fracture apertures so the minimum width is set to  $w_{min} = 10^{-8}$  to avoid convergence issues that a smaller width constraint would entail due to round-off errors. Containment to a rectangular footprint is also ensured by the appropriate choice of layered fracture toughness (Mori *et al.* 2024). This parameter set corresponds to the dimensionless shut-in time  $\omega \sim 5.9 \times 10^{-3}$  and arrest regime parameter  $\bar{\phi}^V \sim 1.9571 \times 10^3$  (see § 5 for the definition and interpretation of these parameters).

In the top plot in figure 4, we compare the first quadrant projections of the ILSA-PL3D (dashed red) and IMMA-PKN (solid black) pre-arrest footprints. Because both  $x$  and  $y$  axes are scaled to the factor  $H/2$ , the sequence of footprints represent the evolving

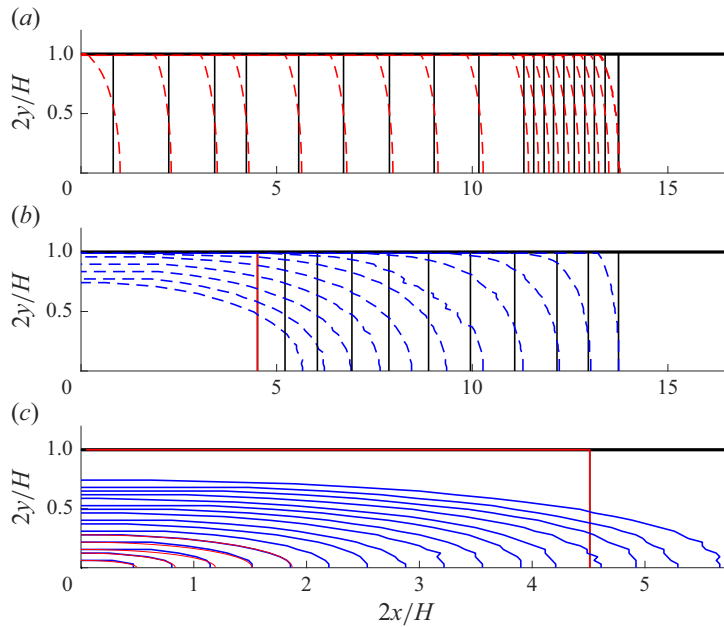


Figure 4. (a) pre- and post-shut-in IMMA-PKN (solid black) and ILSA-PL3D (dashed red) fracture footprints before arrest. (b) receding IMMA-PKN (solid black) and ILSA-PL3D (dashed blue) fracture footprints up till the point of collapse of the PKN solution, (c) ILSA-PL3D (solid blue) fracture footprints subsequent to the PKN collapse.

aspect ratio  $2\ell/H$ . The aspect ratio at shut-in is approximately  $2\ell_s/H \sim 11.44$ , while after shut-in the fracture continues to propagate until arrest when the aspect ratio is approximately  $2\ell_a/H \sim 13.74$ . In the middle plot in figure 4, we compare the receding fracture fronts of the ILSA-PL3D (dashed blue) and IMMA-PKN (solid black) algorithms. In contrast to the nearly vertical fronts of the propagating ILSA-PL3D fracture footprints shown in the top plot, the receding ILSA-PL3D fracture fronts become more curved as recession progresses. These receding ILSA-PL3D fracture footprints eventually separate from the original containment rectangle when  $2\ell/H \sim 8.5$  and ultimately assume a more elliptic shape. While the IMMA-PKN fracture fronts initially follow the maximum points of the corresponding fracture fronts for the ILSA-PL3D model, they ultimately approximate an averaged front position such that the fracture volume matches that of the fully planar model. The red vertical line in the middle plot when  $2\ell/H \sim 4.5$  represents the last recession front of the PKN model before collapse. In the numerical IMMA-PKN simulations, an efficiency threshold  $\eta < 0.5\%$  was used as an objective criterion to identify the collapse time. It is typically not possible for the IMMA-PKN model to remain stable beyond the efficiency threshold.

In the bottom plot in figure 4, we render the ILSA-PL3D fracture footprints (solid blue) as well as the last recession front of the PKN model, which is the same red vertical line shown in the middle figure. Since the width constraint logic used in the ILSA-PL3D model has been carefully calibrated, we assume that it provides an accurate capture of the dynamics of the receding fracture. Given that the PKN model is constrained to a rectangular geometry, and cannot faithfully capture the significant topological changes of the ILSA-PL3D model once it separates from the containment layer boundaries, it is to be expected that the two models deviate beyond this point. Indeed, the PKN front location tries to capture an average position, whose location is set to match the PKN fracture

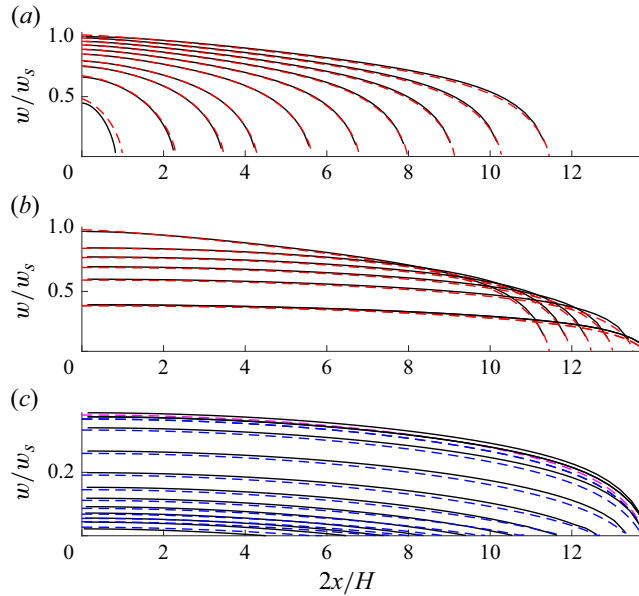


Figure 5. (a) pre-shut-in IMMA-PKN (solid black) and ILSA-PL3D (dashed red) scaled fracture apertures  $w/w_s$  plotted as functions of the scaled distance  $2x/H$  from the injection point. Here  $w_s = w(0, t_s)$  is the aperture at the well-bore at the time of shut-in  $t_s$ . (b) post-shut-in scaled fracture apertures. (c) scaled receding fracture apertures for the IMMA-PKN (solid black) and ILSA-PL3D (dashed blue) algorithms sampled up to the point of collapse of the PKN model.

volume to that of the fully curved fracture ILSA-PL3D model. Since the PKN model significantly over-estimates the fracture footprint, to maintain volume balance it is forced to under-estimate the fracture aperture, which, in turn, leads to an earlier estimate of the collapse time. In contrast, the PL3D model has the freedom to model the non-rectangular post-separation fracture footprints and is, therefore, able to capture the dynamics of the HF much closer to the point of collapse.

We see that these PL3D recession fronts, which persist beyond the collapse of the PKN solution, approach an approximately elliptic shape. For the last five such elliptical fracture footprints, we also represent by solid red curves the ellipses whose semi-major axes correspond to the fracture lengths and whose semi-minor axes correspond to the fracture heights. We observe that these red ellipses are almost indistinguishable from the PL3D fracture footprints, which are represented by the solid blue lines.

In the top plot in figure 5, we compare the pre-shut-in fracture apertures for the IMMA-PKN (solid black) and ILSA-PL3D (dashed red) solutions. In the middle plot, we compare the post-shut-in fracture apertures representing the propagation up to the point of arrest. In the bottom plot, the dashed magenta curve represents the ILSA-PL3D solution during the brief period during which the fracture continues to deflate while arrested, while the corresponding IMMA-PKN solution is represented by a solid black curve. The dashed blue curves represent the ILSA-PL3D fracture apertures while the corresponding IMMA-PKN fracture apertures are represented by the solid black curves. The last of these receding fracture aperture comparisons is sampled just before the collapse of the IMMA-PKN model. We observe that the IMMA-PKN and ILSA-PL3D fracture apertures represented in figure 5 show close agreement.

In the top left plot in figure 6, we compare the scaled fracture dimensions for the IMMA-PKN and ILSA-PL3D solutions as functions of the scaled time  $t/t_s$ . The horizontal

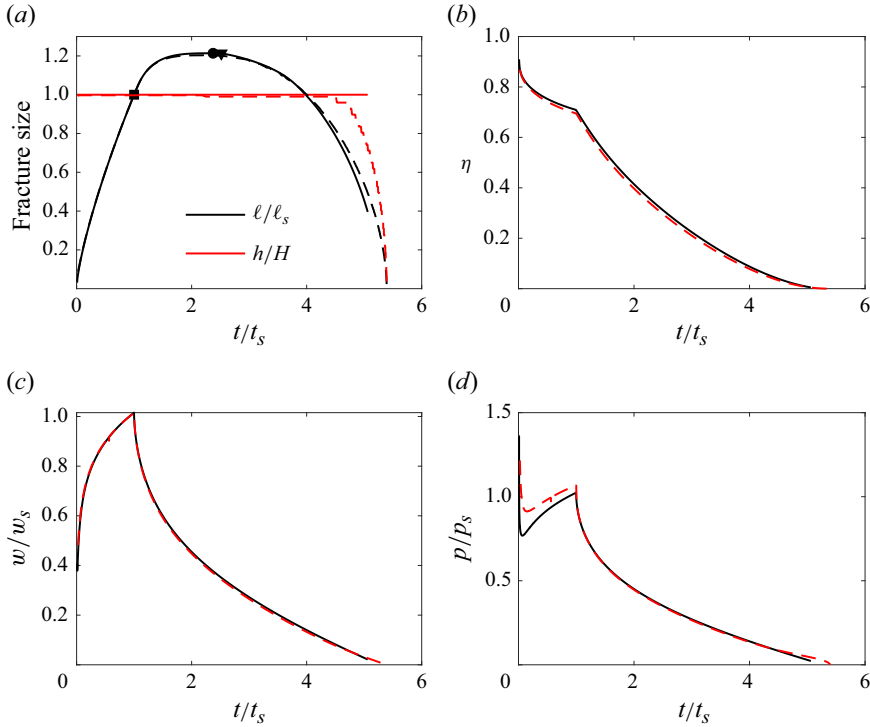


Figure 6. The IMMA-PKN solution is represented by (solid) curves and the ILSA-PL3D solution by (dashed) curves. Here  $\ell_s$ ,  $w_s$ ,  $p_s$ , are the fracture half-length, and aperture and pressure at the injection point all sampled at the time of shut-in  $t_s$ . Moreover,  $h$  represents the vertical dimension of the fracture at the injection point: for the PKN model  $h = H$ , while for the PL3D model  $h \leq H$ . Before the PL3D fracture reaches the constraining layers  $h < H$  briefly, followed by  $h = H$ , and finally the PL3D fracture retreats from the constraining layers and  $h < H$  once again (designated by the red dashes). (a) scaled fracture dimensions, (b) fracture efficiency  $\eta$ , (c) scaled fracture aperture at the injection point  $w/w_s$ , (d) scaled fluid pressure at the injection point  $p/p_s$ , all plotted as functions of the scaled time  $t/t_s$ .

dimension is determined by the scaled fracture length  $\ell/\ell_s$ , which is represented by the solid black curve for the PKN model and the dashed black curve for the PL3D model. On the  $\ell/\ell_s$  vs  $t/t_s$  plot, the shut-in time is represented by the solid black square ■, the arrest point is represented by the solid black circle ●, while the point of initiation of recession is represented by the solid black triangle ▼. The vertical dimension is determined by the scaled fracture height  $h/H$ , which is represented by the solid red curve for the PKN model and the dashed red curve for the PL3D model. The separation time  $t/t_s \sim 4.5$  at which the dashed red curve deviates from the solid red curve, represents the time at which the PL3D fracture footprint first loses contact with the confining layers  $y = \pm H/2$ . The fracture efficiency  $\eta$  as a function of time is plotted in the top right figure. The scaled fracture aperture at the injection point  $w/w_s$  is plotted as a function of time in the bottom left plot, while the scaled fluid pressure  $p/p_s$  at the injection point is plotted as a function of time in the bottom right plot.

## 5. Scaling analysis

### 5.1. Scaling for a PKN fracture subject to a constant injection rate $Q_0$

Following Detournay (2004, 2016) we introduce a length scale  $l_*$ , time scale  $t_*$ , and characteristic aperture  $w_*$  and net pressure  $p_*$  such that  $x = l_*\xi$ ,  $t = t_*\tau$ ,  $\bar{w} = w_*\Omega$ ,

and  $p = p_* \Pi$  into the governing equations (2.6) and (2.13), enabling us to identify the following five dimensionless groups:

$$\mathcal{G}_s = \frac{l_* H w_*}{Q_0 t_*}, \quad \mathcal{G}_m = \frac{l_* \bar{\mu} Q_0}{w_*^3 p_* H}, \quad \mathcal{G}_c = \frac{C' l_* H}{t_*^{1/2} Q_0}, \quad \mathcal{G}_e = \frac{\bar{E} w_*}{H p_*}, \quad \text{and} \quad \mathcal{G}_k = \frac{\bar{K}}{\sqrt{H} p_*}. \quad (5.1)$$

The storage-viscosity  $m$ -scaling can be identified by requiring  $\mathcal{G}_s = \mathcal{G}_m = \mathcal{G}_e = 1$ , from which it follows that the length  $l_m$ , aperture  $w_m$  and pressure  $p_m$  scales are respectively given by

$$l_m = \left( \frac{\bar{E} Q_0^3 t^4}{\bar{\mu} H^4} \right)^{1/5} \quad w_m = \left( \frac{\bar{\mu} Q_0^2 t}{\bar{E} H} \right)^{1/5} \quad \text{and} \quad p_m = \left( \frac{\bar{E}^4 \bar{\mu} Q_0^2 t}{H^6} \right)^{1/5}, \quad (5.2)$$

while the dimensionless toughness and leak-off coefficients become

$$\mathcal{G}_k := \mathcal{K}_m(t) = \left( \frac{\bar{t}_{km}}{t} \right)^{1/5} \quad \text{and} \quad \mathcal{G}_c := \mathcal{C}_m(t) = \left( \frac{t}{\bar{t}_{m\tilde{m}}} \right)^{3/10}, \quad (5.3)$$

where  $\bar{t}_{km} = (\bar{K}^5 H^{7/2}) / (\bar{E}^4 \bar{\mu} Q_0^2)$  and  $\bar{t}_{m\tilde{m}} = (\bar{\mu} Q_0^2 / \bar{E} C'^5 H)^{2/3}$  are the  $k$ - $m$  and  $m$ - $\tilde{m}$  transition time scales, respectively.

We define the propagation mode parameter to be the ratio of these two characteristic time scales

$$\bar{\phi} = \frac{\bar{t}_{km}}{\bar{t}_{m\tilde{m}}} = \left( \frac{\bar{K}^6 H^5 C'^4}{\bar{\mu}^2 \bar{E}^4 Q_0^4} \right)^{5/6}. \quad (5.4)$$

The leak-off ( $\tilde{m}$ -scaling) can be obtained by requiring  $\mathcal{G}_c = 1$  instead of  $\mathcal{G}_s$

$$l_{\tilde{m}} = \frac{Q_0 t^{1/2}}{H C'} \quad w_{\tilde{m}} = \left( \frac{\bar{\mu} Q_0^2}{\bar{E} H C'} \right)^{1/4} t^{1/8} \quad \text{and} \quad p_{\tilde{m}} = \left( \frac{\bar{E}^3 \bar{\mu} Q_0^2}{H^5 C'} \right)^{1/4} t^{1/8}, \quad (5.5)$$

while the dimensionless toughness and storage coefficients become

$$\mathcal{G}_k := \mathcal{K}_{\tilde{m}}(t) = \left( \frac{\bar{t}_{k\tilde{m}}}{t} \right)^{1/8} \quad \text{and} \quad \mathcal{G}_s := \mathcal{S}_{\tilde{m}}(t) = \left( \frac{\bar{t}_{m\tilde{m}}}{t} \right)^{3/8}, \quad (5.6)$$

where  $\bar{t}_{k\tilde{m}} = (\bar{K}^8 H^6 C'^2) / (\bar{E}^6 \bar{\mu}^2 Q_0^4)$ . The toughness ( $k$ -scaling) can be obtained by requiring  $\mathcal{G}_k = 1$  instead of  $\mathcal{G}_m$ , and the toughness-leak-off ( $\tilde{k}$ -scaling) can be obtained by requiring  $\mathcal{G}_k = 1$  and  $\mathcal{G}_c = 1$  see (Dontsov 2022).

## 5.2. Characteristic power laws for arrest

In this paper we consider the injection of fluid at a constant flux  $Q_0$  followed by shut-in at a certain time  $t_s$ . Propagation of the HF, initiated at the beginning of the injection phase, may continue after shut-in depending on the regime of propagation. A propagating fracture in a permeable medium will ultimately come to rest either due to excessive leak-off if  $\bar{K} = 0$  or because the stress intensity factor  $K$  has dropped below the fracture toughness when  $\bar{K} > 0$ . There is an arrest period during which  $K$  decreases as the fracture continues to lose fluid to the porous medium so that  $\dot{w} < 0$ , until transition to the recession asymptote is initiated when  $K = 0$  and the fracture starts to recede. However, if the HF is already in the leak-off regime at the time of shut-in, then recession can be expected to start almost immediately after arrest.

The appropriate scaling for the dynamics with a fixed injected volume  $V_0$  can be obtained Mori & Lecampion (2021) directly from those of a fracture driven by a constant flux  $Q_0$  given in (5.2) by making the simple substitution  $Q_0 = V_0/t$ . In this case the length  $l_m^V(t)$  and aperture  $w_m^V(t)$  scales are given by

$$l_m^V(t) = \left( \frac{\bar{E} V_0^3 t}{\bar{\mu} H^4} \right)^{1/5} \quad \text{and} \quad w_m^V(t) = \left( \frac{\bar{\mu} V_0^2}{\bar{E} H t} \right)^{1/5}, \quad (5.7)$$

while the dimensionless toughness  $\mathcal{K}_m^V(t)$  and leak-off  $\mathcal{C}_m^V(t)$  parameters become

$$\mathcal{K}_m^V(t) = \left( \frac{t}{\bar{t}_{mk}^V} \right)^{1/5} \quad \text{and} \quad \mathcal{C}_m^V(t) = \left( \frac{t}{\bar{t}_{m\tilde{m}}^V} \right)^{7/10}, \quad (5.8)$$

where  $\bar{t}_{mk}^V = (\bar{E}^4 \bar{\mu} V_0^2) / (\bar{K}^5 H^{7/2})$  and  $\bar{t}_{m\tilde{m}}^V = ((\bar{\mu}^2 V_0^4) / (\bar{E}^2 C'^{10} H^2))^{1/7}$  are the  $m-k$  and  $m-\tilde{m}$  transition time scales associated with the post-shut-in dynamics of a PKN HF, respectively.

In order to characterise the modes of arrest, we define the following arrest regime parameter  $\bar{\phi}^V$  for a fixed injected volume PKN HF to be:

$$\bar{\phi}^V = \frac{\bar{t}_{mk}^V}{\bar{t}_{m\tilde{m}}^V} = \left( \frac{\bar{\mu}^2 \bar{E}^{12} C'^4 V_0^4}{\bar{K}^{14} H^9} \right)^{5/14}. \quad (5.9)$$

Once shut-in has occurred the two transition times defined in (5.8) identify two different ways the fracture behaves after the time of arrest  $t_a$ , which, if  $\bar{K} > 0$ , is characterised by the stress intensity factor dropping below the critical fracture toughness and, as a result, the velocity of the fracture going to zero. If  $t_a \sim \bar{t}_{mk}^V \ll \bar{t}_{m\tilde{m}}^V$ , so that  $\bar{\phi}^V \ll 1$ , then at the time of arrest, the fracture is propagating in the toughness regime and still contains a significant amount of fluid that needs to leak-off before recession can start. In this case, there will be a significant period during which the fracture deflates while it is in a state of arrest after which recession will begin. Conversely, if  $t_a \sim \bar{t}_{m\tilde{m}}^V \ll \bar{t}_{mk}^V$ , so that  $\bar{\phi}^V \gg 1$ , then at the time of arrest the fracture is propagating in the leak-off regime and has lost sufficient fluid to preclude significant further propagation of the fracture. In this case, recession can be expected to start almost immediately and there will be a very short arrest period. We observe that the parameter  $\bar{\phi}^V$  defined in (5.9) has no meaning in the zero toughness case since  $\bar{t}_{mk}^V = \infty$ .

In the analysis that follows we consider a given shut-in time  $t_s$ , which we define with respect to the constant injection rate storage-leak-off transition time  $\bar{t}_{m\tilde{m}}$  in terms of the parameter  $\omega$  defined by

$$\omega = \frac{t_s}{\bar{t}_{m\tilde{m}}}. \quad (5.10)$$

At shut-in, the injected volume is  $V_s = Q_0 t_s$ , the dimensionless leak-off coefficient  $\mathcal{C}_m(t_s) := \mathcal{C}_s = \omega^{3/10}$ , while the dimensionless toughness  $\mathcal{K}_m(t_s) := \mathcal{K}_s = (\bar{\phi})^{1/5} \omega^{-1/5}$ . The fixed injected volume transition times, at which  $\mathcal{K}_m^V(t) = 1$  and  $\mathcal{C}_m^V(t) = 1$ , can be expressed in terms of  $\mathcal{K}_s$  and  $\mathcal{C}_s$  as follows:

$$\bar{t}_{mk}^V := t_s \mathcal{K}_s^{-5} \quad \text{and} \quad \bar{t}_{m\tilde{m}}^V := t_s \mathcal{C}_s^{-10/7}. \quad (5.11)$$

Now, making use of the transition times defined in (5.3) and (5.8) as well as the definition (5.9) of the arrest regime parameter  $\bar{\phi}^V$ , the following relationship can be



established between the fixed injected volume transition times  $\bar{t}_{m\tilde{m}}^V$  and  $\bar{t}_{mk}^V$  and the dimensionless shut-in parameter  $\omega$ :

$$\bar{t}_{m\tilde{m}}^V = t_s \omega^{-\frac{3}{7}} \quad \text{and} \quad \bar{t}_{mk}^V = \bar{\phi}^V t_s \omega^{-\frac{3}{7}}. \quad (5.12)$$

Naturally, because of the definition of the regime parameter  $\bar{\phi}^V$  in (5.9), both the transition times  $\bar{t}_{m\tilde{m}}^V$  and  $\bar{t}_{mk}^V$  have the same power law dependence on  $\omega$ . If  $\omega \ll 1$ , then, at the time of shut-in  $t_s$ , the fracture is still propagating in the viscous-storage regime well away from the leak-off regime, so the arrest time  $t_a$  is determined by the transition times  $\bar{t}_{mk}^V$  if  $\bar{K} > 0$  or by  $\bar{t}_{m\tilde{m}}^V$  in the zero toughness case. The corresponding asymptotic dependence of the arrest length and arrest aperture can be obtained by substituting these transition times into (5.7). If  $\omega \gg 1$ , then, at the time of shut-in  $t_s$ , the fracture is well into the leak-off regime so arrest occurs almost immediately, i.e.  $t_a \sim t_s$ . Defining  $l_s := l_m(t_s)$  and  $w_s := w_m(t_s)$ , and combining (5.12)<sub>b</sub> with (5.7), we obtain

$$t_a/t_s \sim \begin{cases} \bar{\phi}^V \omega^{-\frac{3}{7}} & \text{if } \omega \ll 1 \\ 1 & \text{if } \omega \gg 1 \end{cases}, \quad (5.13)$$

$$l_a/l_s \sim \begin{cases} (\bar{\phi}^V)^{1/5} \omega^{-3/35} & \text{if } \omega \ll 1 \\ 1 & \text{if } \omega \gg 1 \end{cases}, \quad (5.14)$$

$$w_a/w_s \sim \begin{cases} (\bar{\phi}^V)^{-1/5} \omega^{3/35} & \text{if } \omega \ll 1 \\ 1 & \text{if } \omega \gg 1 \end{cases}. \quad (5.15)$$

For the zero toughness case  $\bar{K} = 0$  the arrest time  $t_a$  will be determined by the transition time  $\bar{t}_{m\tilde{m}}^V$ , which has the same power law as  $\bar{t}_{mk}^V$ , without the factor involving the regime parameter  $\bar{\phi}^V$ . Thus the power law asymptotes for the zero toughness case are identical to those in (5.13)–(5.15) without the factor involving the regime parameter  $\bar{\phi}^V$ .

The IMMA-PKN results for the non-zero toughness case  $K' > 0$  are presented in figure 7. The arrest time to shut-in time (a) and arrest length to shut-in length (b) ratios are plotted as functions of the dimensionless shut-in time  $\omega$  for different values of the regime parameter  $\bar{\phi}^V$ . Here the dashed red line represents the power law  $A\omega^\alpha$  for the particular case  $\bar{\phi}^V = 1957.1$ , with  $A$  and  $\alpha$  computed by a log linear regression of the first few data points. The regression yields  $\alpha = -0.42$  for  $t_a/t_s$ , which is consistent with the power law (5.13), and  $\alpha = -0.0842$  for  $l_a/l_s$ , again consistent with the power law (5.14). In both figures (a) and (b) the  $\bullet$  symbol is used to indicate the curve corresponding to the regime parameter  $\bar{\phi}^V = 100$ , and the curve with the  $\blacktriangle$  symbol corresponds to the regime parameter  $\bar{\phi}^V = 1957.1$ .

### 5.3. Solution landscape represented by the evolving fracture length $\ell$

In table 1, the ratio of the fracture length scaled to the shut-in length  $\ell(t)/\ell_s$  is plotted as a function of the scaled time  $t/t_s$  for a range of different  $\bar{\phi}^V$  and  $\omega$  values. The value of the arrest regime parameter  $\bar{\phi}^V$  is constant for each column of the table while the value of the dimensionless shut-in parameter  $\omega$  is constant for each row. Fracture lengths are plotted for  $\bar{\phi}^V = 10^2$  and  $10^{3.29} \approx 1957.1$  and  $\omega = 10^{-8}$  and  $10^{-2}$ . The initially black parts of the curve represent the dynamics driven by injection up to the shut-in time  $t_s$ , which is designated by a red asterisk  $*$ . The subsequent red part of the curve, between the red shut-in point  $*$  and the magenta arrest point  $\bullet$ , represents the length increase as the fracture continues to propagate between the time fluid injection ceases and the point of arrest.

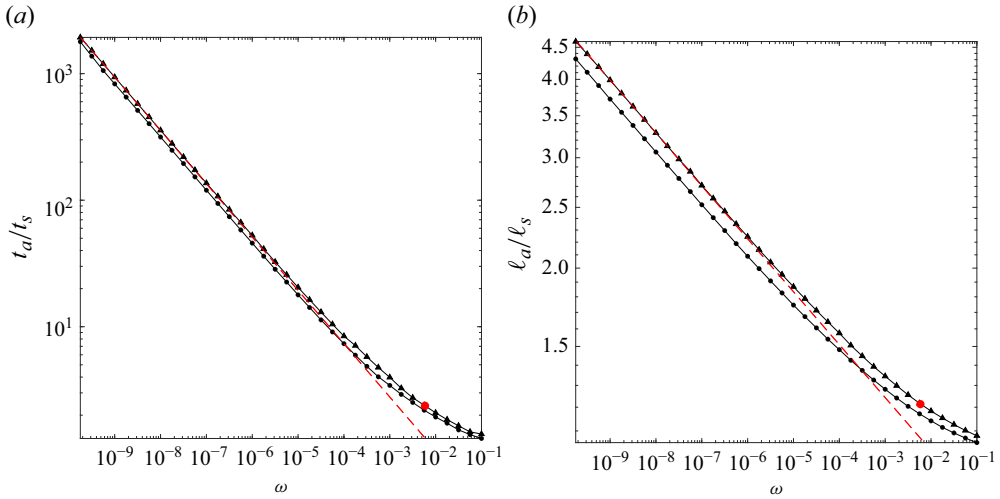


Figure 7. The solid black lines indicate the numerical solutions for (a) the arrest time to shut-in time ratios and (b) the arrest length to shut-in length ratios, both plotted as functions of  $\omega$  for the values of the regime parameter  $\bar{\phi}^V \in \{100 (\bullet), 1957.1 (\blacktriangle)\}$ . The red  $\bullet$  symbols in each plot correspond to the parameter set  $(\omega, \bar{\phi}^V) = (0.0059, 1957.1)$  used in the PyFrac calibration runs in § 4.2. The dashed red lines represent linear regressions of the data set  $(\blacktriangle)$  corresponding to  $\bar{\phi}^V = 1957.1$ , assuming  $t_a/t_s$  and  $\ell_a/\ell_s$  are power laws of the form  $A\omega^\alpha$ .

The magenta part of the curve, between the arrest point  $\bullet$  and the recession initiation point  $\blacktriangledown$ , represents the period during which the fracture continues to lose fluid while at arrest, so that  $V = 0$  and  $\partial w/\partial t < 0$ . The subsequent black part of the curve, starting with  $\blacktriangledown$ , represents the decreasing fracture length  $\ell$  while the fracture recedes. Scanning down the first column  $\bar{\phi}^V = 10^2$ , we observe that the collapse time occurs a factor of 1150 times later than the shut-in time for the case  $\omega = 10^{-8}$ , which is reduced to 4.4 times for the case  $\omega = 10^{-2}$ . Indeed, as  $\omega$  increases, the post shut-in propagation time, arrest period and recession time till collapse all decrease.

## 6. Self-similarity close to closure – the sunset solution

### 6.1. Evidence of self-similarity

In order to motivate the analysis performed in this section we re-plot the data presented in § 4.2 in a form that reveals the self-similar nature of the solution as the fracture approaches the time of collapse  $t_c$ . We recall the dimensionless parameters that characterise this set of data are given by the pair  $(\omega, \bar{\phi}^V) = (0.0059, 1957.1)$ .

In figure 8(a), we plot the scaled fracture length  $\ell/\ell_r$  for the PKN (solid black) and PL3D (solid blue) solutions and the scaled fracture height  $h/H$  for the PL3D solution (solid magenta) vs the scaled reverse time  $(t_c - t)/t_r$ . Here  $\ell_r$  and  $t_r$  are the fracture length and time at which the fracture starts to recede, respectively. The linear trend in the asymptotic limit  $t \rightarrow t_c$  indicates that  $\ell$  behaves like a power law in this limit, i.e.  $\ell \sim A(t_c - t)^\gamma$ . A linear regression on the first few points of each of these curves yields (represented by the dashed red lines) that for the PKN case  $\gamma \approx 0.506$  and for the PL3D case  $\gamma \approx 0.502$ . The exponent for the magenta curve representing the PL3D fracture height is 0.42, which is close to 0.5, indicating that the successive elliptic footprints are close to self-similar as the fracture recedes. In figure 8(b), we plot the PL3D scaled fracture aperture  $w/w_r$  at the injection point (blue curve) as a function of the scaled reverse time  $(t_c - t)/t_r$ . A plot of the PKN aperture is similar, except that the collapse

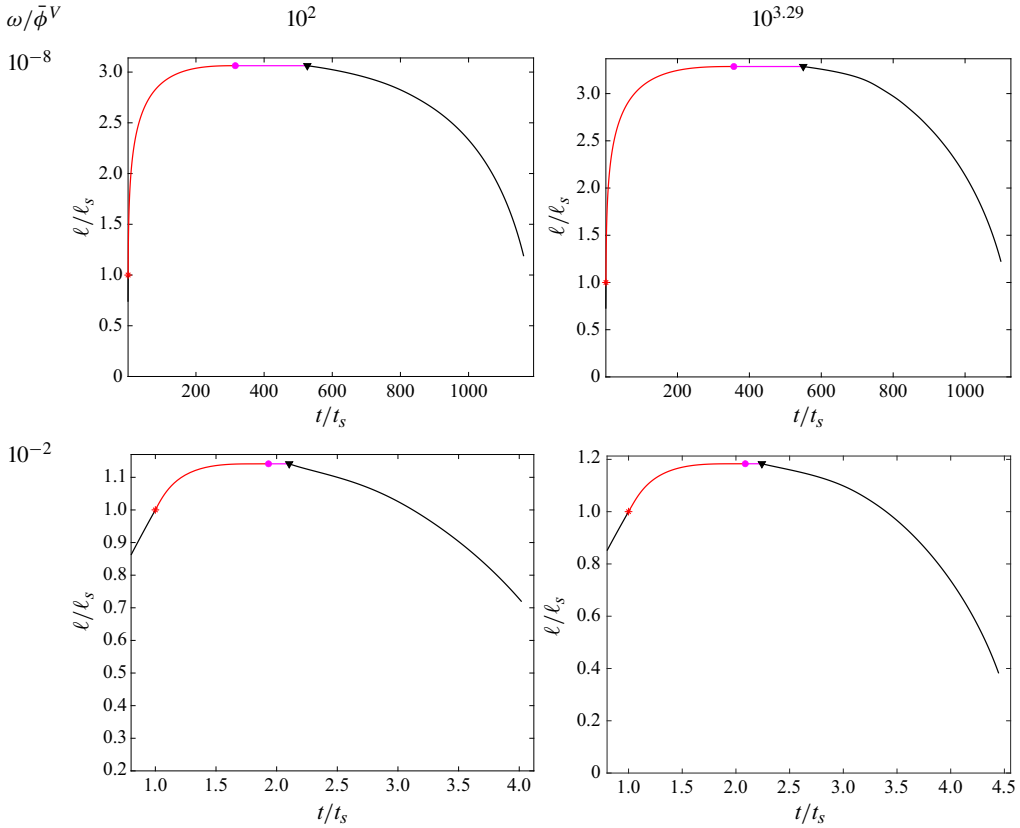


Table 1. Scaled length  $\ell(t)/\ell_s$  vs  $t/t_s$  plotted for different  $\bar{\phi}^V$  and  $\omega$  values. In each of these plots: propagation under injection is represented by the black portion of the curve terminating with the  $*$  symbol; the red portion of the curve, between the  $*$  and the  $\bullet$  symbols, represents post shut-in propagation; the magenta portion of the curve, between the  $\bullet$  and the  $\blacktriangledown$  symbols, represent post shut-in propagation; the black portion of the curve, starting with the  $\blacktriangledown$  symbol, represents recession.

time of the PKN fracture occurs earlier (and at a larger aperture value) than that of the PL3D fracture. To keep the figure uncluttered this plot is not provided. Due to the PKN model being constrained to a rectangular geometry, it is not able to capture the recession process once the closure boundary retreats from the containment layers. We observe that as  $t \rightarrow t_c$  the fracture aperture tends a linear function of time, so that  $w \sim g \times (t_c - t)$ . A linear regression on the first few points of the PL3D curve shown in figure 8(b) yields the gradient  $g \approx 1.73 \times 10^{-7} \text{ ms}^{-1}$ , while from a similar a linear regression of the corresponding PKN curve we obtain the estimate  $g \approx 2.54 \times 10^{-7} \text{ ms}^{-1}$ .

In figure 9, for a sequence of sample times, starting with the recession initiation time  $t_r$ , we plot the dynamically scaled fracture aperture  $w(x, t)/w(0, t)$  against the scaled distance from the injection point  $x/\ell(t)$  for: (a) the PL3D model (blue), and (b) the PKN model (black). We observe that in both cases the fracture apertures approach a universal function of the scaled distance  $x/\ell(t)$ , which is represented by the dashed red curve. Since these dynamic scale factors are precisely the fracture length  $\ell(t)$  for the abscissae and the injection aperture  $w(0, t)$  for the ordinates, both of which exhibit power law behaviour

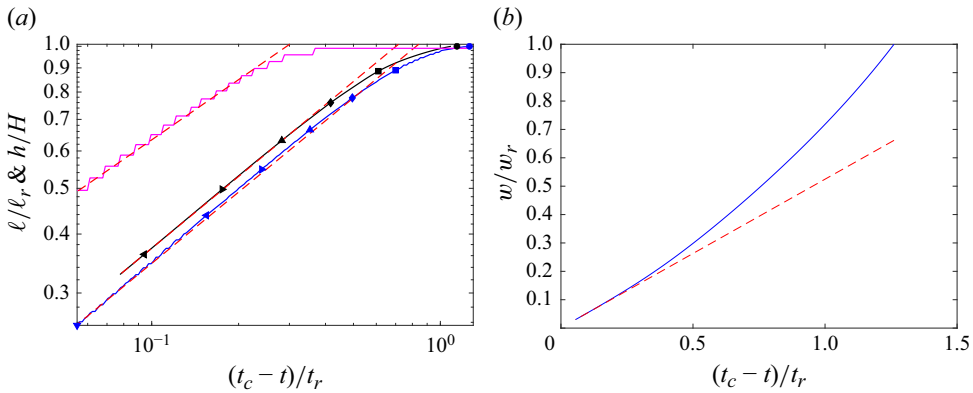


Figure 8. In each of these plots the dashed red lines represent the lines obtained a linear regression on the first few points of each of the curves. (a) Log-log plot of the scaled fracture length  $\ell/\ell_r$  for the PKN (solid black) and PL3D (solid blue) solutions and the scaled fracture height  $h/H$  (solid magenta) vs the scaled reverse time  $(t_c - t)/t_r$ . (b) The solid blue curve represents the PL3D scaled fracture aperture at the injection point  $w/w_r$  vs the scaled reverse time  $(t_c - t)/t_r$ .

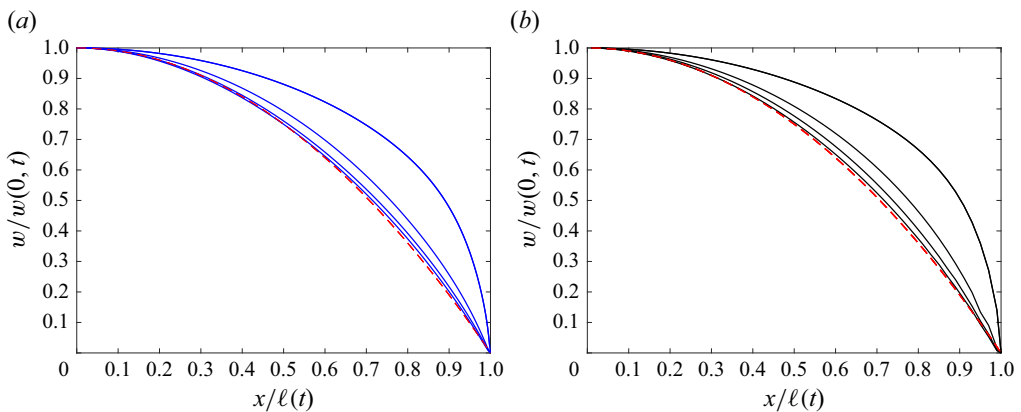


Figure 9. (a) Scaled PL3D fracture aperture  $w(x, t)/w(0, t)$  vs the scaled distance from the injection point  $x/\ell(t)$ . (b) Scaled PKN fracture aperture  $w(x, t)/w(0, t)$  vs the scaled distance from the injection point  $x/\ell(t)$ . The dashed red curve represents the universal aperture to which the scaled numerical solutions tend as  $t \rightarrow t_c$ .

according to figure 8, there is strong evidence of the existence of a similarity solution for both the PL3D model and the PKN model.

## 6.2. Reverse-time equations and the similarity ansatz

The evidence presented in § 6.1 indicates that the both the PL3D and PKN models for receding rectangular fractures ultimately tend to a self-similar structure. Though the PL3D equations are much more complex and not amenable to analysis, it is possible to analyse the PKN equations to investigate the nature of this self-similar behaviour, which is what we explore in the remainder of this section. Given the focus on the behaviour of the solution close to the closure time  $t_c$ , to simplify the analysis we rewrite the governing equations in terms of the reverse time  $t' = t_c - t$ . In this case,  $\dot{\ell}(t') > 0$  for recession, the elasticity equation (3.1) remains unchanged, while the signs are changed in the last two terms in (3.2). As the HF approaches collapse, the current time  $t$  is assumed to be sufficiently more

advanced than the initiation times active in the collapsing fracture, i.e.  $t \gg t_0(s, t)$ , that the leak-off term has the following asymptotic behaviour:

$$\hat{g}(\hat{s}, t) = \frac{C'}{\sqrt{t - t_0(\ell(1 - \hat{s}))}} \stackrel{t \gg t_0}{\sim} \frac{C'}{\sqrt{t}}. \quad (6.1)$$

Thus for sufficiently advanced times  $t$ , the leak-off function  $\hat{g}(\hat{s}, t)$  is slowly varying in time and approximately independent of  $\hat{s}$ , so that the leak-off function  $\hat{g}$  may be considered to be approximately constant. Thus, in what follows,  $\hat{g}$  is replaced by the constant  $\hat{g}_0$ . The lubrication equation (3.2), expressed in terms of the reverse time  $t'$ , becomes

$$\frac{\partial \hat{w}}{\partial t'} + (1 - \hat{s}) \frac{\ell}{\ell} \frac{\partial \hat{w}}{\partial \hat{s}} = - \frac{1}{\bar{\mu} \ell^2} \frac{\partial}{\partial \hat{s}} \left( \hat{w}^3 \frac{\partial \hat{p}}{\partial \hat{s}} \right) + \hat{g}_0. \quad (6.2)$$

We observe that these reverse-time equations are equivalent to those of an inflating fracture subjected to a constant source distributed throughout its growing length.

Motivated by the evidence presented in figures 8 and 9, and the accompanying observations made in § 6.1, we look for a similarity solution to this ‘growing’ HF driven by an influx of fluid from a constant distributed source in terms of  $s = x/\ell(t')$  and by assuming a solution of the form

$$\bar{w}(s, t') = t'^{\alpha} W(s) \quad p(s, t') = t'^{\beta} P(s) \quad \ell(t') = \Lambda t'^{\gamma}. \quad (6.3)$$

Note that for the reverse time,  $t' = 0$  represents the time of closure.

### 6.3. Fracture volume

Define the average fracture aperture  $\mathcal{W}$  to be

$$\mathcal{W} = \int_0^1 \bar{w}(s, t') ds = t'^{\alpha} \int_0^1 W(s) ds = t'^{\alpha} \bar{W}. \quad (6.4)$$

The crack volume  $V_c$  can be expressed in terms of the similarity variables as follows:

$$V_c(t) = \mathcal{W} \ell = \Lambda t'^{\alpha+\gamma} \bar{W}. \quad (6.5)$$

Since the rate of change of volume should match the rate of efflux of fluid, it follows that

$$\dot{V}_c = \Lambda(\alpha + \gamma) t'^{\alpha+\gamma-1} \bar{W} = g_0 \ell = g_0 \Lambda t'^{\gamma}. \quad (6.6)$$

Matching powers we obtain the following:

$$\alpha = 1 \quad \text{and} \quad \bar{W} = \frac{g_0}{1 + \gamma}. \quad (6.7)$$

### 6.4. Tip asymptotics and Taylor expansion

Now  $\bar{w}(s, t') = \hat{w}(\hat{s}, t') = t' W(s) = t' W(1 - \hat{s})$  and, motivated by the linear asymptote in (3.20), we assume a Taylor expansion for  $W$  about  $s = 1$  in powers of  $\hat{s}$  of the form

$$\hat{w}(\hat{s}, t') = t' \sum_{n=1}^{\infty} \frac{(-1)^n w_n}{n!} \hat{s}^n, \quad (6.8)$$

where  $w_n = (d^n W / ds^n)|_{s=1}$  and  $w_0 = W(1) = 0$ .

Taking time and space derivatives of (6.8), the left side of (6.2) can be written in the form

$$\frac{\partial \hat{w}}{\partial t'} + (1 - \hat{s}) \frac{\ell}{\ell} \frac{\partial \hat{w}}{\partial \hat{s}} = -\gamma w_1 + \sum_{n=1}^{\infty} (-1)^n \frac{(1 - n\gamma)w_n - \gamma w_{n+1}}{n!} \hat{s}^n. \quad (6.9)$$

Now because the asymptotic behaviour of the non-local kernel function  $G((\hat{s}' - \hat{s})/\varepsilon)$  changes depending on the distance between the sending point  $\hat{s}'$  and the receiving point  $\hat{s}$ , in order to determine the asymptotic behaviour of the pressure  $\hat{p}$ , it is necessary to split the action of integral operator into an inner region in which the receiving point is close to the tip  $\hat{s} < \varepsilon$ , and an outer region for which the receiving point is remote from the tip  $\hat{s} > \varepsilon$ .

Inner region: using (3.10) to determine the leading behaviour for the pressure  $\hat{p}$  from the action of the Cauchy operator on the leading term in (6.8), it follows that

$$\hat{p}^{\hat{s} \ll \varepsilon} \sim -\frac{\bar{E} t'^{1-\gamma}}{2\pi\Lambda} w_1 \ln \hat{s}. \quad (6.10)$$

Comparing (6.3) and (6.10) it follows that the time exponent of the pressure  $\beta$  is given by

$$\beta = 1 - \gamma. \quad (6.11)$$

Using the expansion (6.10) for the pressure, the leading behaviour of the flux gradient in the tip region  $\hat{s} < \varepsilon$  can be shown to be of the form

$$\frac{1}{\ell^2} \frac{\partial}{\partial \hat{s}} \left( \frac{\hat{w}^3}{\bar{\mu}} \frac{\partial \hat{p}}{\partial \hat{s}} \right) \sim \frac{\bar{E} t'^{4-3\gamma}}{\pi \bar{\mu} \Lambda^3} w_1^4 \hat{s}. \quad (6.12)$$

Outer region: away from the tip  $\hat{s} > \varepsilon$ , the leading behaviour for the pressure  $\hat{p}$  is given by

$$\hat{p}(\hat{s}, t) \sim \frac{\bar{E}}{H} \hat{w}(\hat{s}, t), \quad (6.13)$$

so the leading behaviour of the flux gradient away from the tip can be shown to be of the form

$$\frac{1}{\ell^2} \frac{\partial}{\partial \hat{s}} \left( \frac{\hat{w}^3}{\bar{\mu}} \frac{\partial \hat{p}}{\partial \hat{s}} \right) \sim \frac{\bar{E} t'^{4-2\gamma}}{\bar{\mu} \Lambda^2 H} 3w_1^4 \hat{s}^2. \quad (6.14)$$

Numerical evidence suggests that, as the fracture approaches closure it accelerates rather than slowing down, which implies that  $\gamma < 1$ . Thus, in the small time limit  $t' \ll 1$ , it follows that  $t'^{4-3\gamma} \ll 1$  and, *a fortiori*,  $t'^{4-2\gamma} \ll 1$ , so we can neglect the flux term on the right of (6.2). The significance of the emerging subdominance of the pressure gradient terms in (6.2) in the limit  $t' \ll 1$  is profound as it signifies a decoupling of the elastic force balance equation from the fluid conservation equation, so that the remaining dominant terms in (6.2) essentially enforce a local kinematic condition between the fluid leak-off velocity and the rate of decrease of the aperture and length of the receding fracture.

Now matching the powers of  $\hat{s}$  in (6.9) to the only non-zero term  $\hat{g}_0$  on the right side of (6.2) (assuming that the flux terms are negligible on this time scale), we obtain the following value for  $w_1$  and recursion for  $w_n$ ,  $n > 1$ :

$$w_1 = -\hat{g}_0/\gamma, \text{ and } w_{n+1} = \frac{(1 - n\gamma)}{\gamma} w_n. \quad (6.15)$$

From this recursion it follows that

$$w_n = -(1 - \gamma)(1 - 2\gamma) \dots (1 - (n - 1)\gamma) \hat{g}_0/\gamma^n. \quad (6.16)$$

Substituting these values for  $w_n$  into (6.8) we obtain the following expansion for  $\hat{w}(\hat{s}, t')$ :

$$\hat{w}(\hat{s}, t') = \hat{g}_0 t' \left[ \frac{1}{\gamma} \hat{s} + \sum_{n=2}^{\infty} \frac{(-1)^{n+1} (1-\gamma)(1-2\gamma) \dots (1-(n-1)\gamma)}{n! \gamma^n} \hat{s}^n \right]. \quad (6.17)$$

Note that the power series (6.17) provides a local solution centred on the fracture tip, which only converges for  $\hat{s} < 1$  and will not yield a global solution valid at the centre of the fracture  $\hat{s} = 1$ . However, we observe from (6.17) that, for  $\gamma < 1$ , there are a countable infinity of global solutions valid for  $0 \leq \hat{s} \leq 1$ , each corresponding to the reciprocals  $\gamma = 1/2, 1/3, \dots, 1/N, \dots$  of the integers greater than or equal to 2, which terminate for finite  $N$  to polynomial solutions. Indeed, for  $\gamma = 1/N$ ,  $N \geq 2$  the series solution (6.17) terminates after  $N$  terms to yield the globally valid solution of degree  $N$

$$\hat{w}(\hat{s}, t') = \hat{g}_0 t' (-1)^N [1 - (1 - \hat{s})^N]. \quad (6.18)$$

From (6.18) we observe that the solutions for  $N$  odd are a-physical since, if this were the case  $\hat{w}(\hat{s}, t) < 0$ , so only solutions with even powers of  $N$  are admissible. Furthermore, from (6.18) we also see that the spatial derivative for all these polynomial solutions satisfy the symmetry condition  $(\partial \hat{w} / \partial \hat{s})(1, t) = 0$  and have  $N - 1$  derivatives that vanish at the centre of the fracture  $\hat{s} = 1$ . The gradient at the fracture tip  $(\partial \hat{w} / \partial \hat{s})(0, t') = \hat{g}_0 t' (-1)^N N$  increases with  $N$  so, of these even polynomials, the solution corresponding to  $\gamma = 1/2$  is the last remaining admissible shape as the fracture approaches closure. Thus the polynomial associated with  $\gamma = 1/2$  forms an attractor for the receding fracture solution, which we call the sunset solution.

## 6.5. The sunset solution

### 6.5.1. Closed form expression for the sunset solution

The similarity solution corresponding to  $\gamma = 1/2$ , when expressed as a function of  $s$ , is given by

$$\bar{w}(s, t') = \hat{g}_0 t' (1 - s^2), \quad s = x/\ell, \quad \ell = \Lambda t'^{1/2}. \quad (6.19)$$

It is interesting to note that slowly draining gravity currents through a layered porous medium also exhibit similarity solutions with a parabolic structure (Prichard *et al.* 2001).

The asymptotic behaviour of the pressure  $p$  can be determined by substituting (6.19) into (2.6) and using the asymptotic behaviour of the kernel  $G$  given in (2.9)

$$p_{PKN}(s, t) = \begin{cases} \frac{t' \bar{E} \hat{g}_0}{H} (1 - s^2) & \text{for } |1 - s| > \varepsilon \\ \frac{t' \bar{E}}{2\pi \Lambda t'^{1/2}} \frac{\hat{g}_0}{|V|} \ln |1 - s| & \text{for } |1 - s| < \varepsilon. \end{cases} \quad (6.20)$$

Since  $\gamma = 1/2$  for the sunset solution, it follows from (6.11) that the time exponent for the pressure  $\beta = 1 - \gamma = 1/2$ , which is consistent with (6.20)<sub>b</sub>, in which the similarity solution for the fracture half-length  $\ell = \Lambda t'^{1/2}$  has been used. In order to close the solution to the forward problem for a receding HF with initial conditions (2.15), the only remaining parameter to specify is the prefactor  $\Lambda$  in the power law for  $\ell$  defined in (6.3).

In figure 10, we plot the scaled fracture apertures  $w/w_s$  against the scaled distance from the injection point  $x/\ell_s$  for (a) the PL3D solution coloured blue and (b) the PKN solutions coloured black compared with the corresponding sunset solutions, which are designated by the dashed red curves. In both plots (a) and (b) the different symbols labelling each curve correspond to the times indicated by the corresponding symbols in figure 8(a).



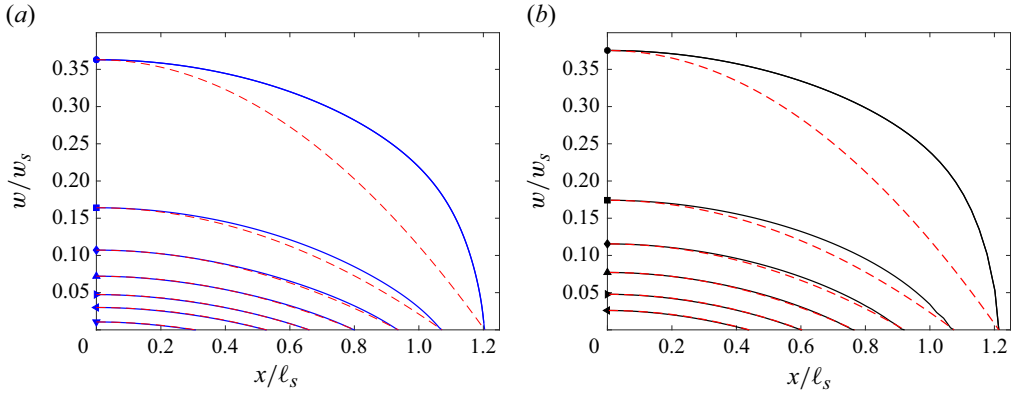


Figure 10. Comparison of the receding (a) PL3D and (b) PKN solutions and the sunset solution for different sample times.

### 6.5.2. Estimation of the leak-off coefficient $C'$

In the analysis to establish the sunset solution for plane strain and radial fractures (Peirce & Detournay 2022a), it was recognised that by determining the time derivative  $\partial \bar{w} / \partial t'$  at the injection point as the fracture approaches collapse, i.e.  $t' \rightarrow 0$ , we can obtain an estimate of  $\hat{g}_0$ , which, according to (6.19), is given by the coefficient of the aperture profile that can be determined by linear regression of the aperture vs  $t'$  function. Thus as the fracture approaches collapse,  $t \rightarrow t_c \gg t_0(\hat{x})$  and (6.1) yields the following estimate for the leak-off coefficient  $C'$ :

$$C' \sim \hat{g}_0 \times \sqrt{t_c}. \quad (6.21)$$

Using (6.21) and the estimate of  $\hat{g}_0$  obtained from the linear regression in figure 8(b), we obtain the estimate  $C' \approx 3.97 \times 10^{-3} \text{ ms}^{-1/2}$ , whereas the value actually used in the simulation was  $C' \approx 3.9516 \times 10^{-3} \text{ ms}^{-1/2}$ .

## 7. Conclusions

The plane strain, radially symmetric, and PKN HF models are much more amenable to analysis than their fully planar counterparts with arbitrary fracture footprints, because of they involve only one spatial dimension. Previous work has established the full set of plane strain asymptotes for HF propagation (Detournay 2004; Garagash *et al.* 2011; Dontsov & Peirce 2015b; Detournay 2016), while (Peirce & Detournay 2022b) established the asymptotes for deflation during arrest and recession. An important result is that these plain strain asymptotes also hold within the tip of any planar fracture with a smooth fracture boundary (Peirce & Detournay 2008). The relatively recent (Adachi & Peirce 2008) formulation of the non-local elasticity equation for the PKN model, has enabled the PKN formulation to be extended to toughness dominated propagation. However, hitherto, there has not been a comprehensive analysis of the full range of asymptotes for the PKN model. In this paper, we have identified an appropriate procedure to transform the governing equations for a steady semi-infinite PKN fracture to be formally identical to those for a steady semi-infinite plane strain fracture. This transformation procedure makes it possible to use the plane strain asymptotes to directly determine the following PKN asymptotes for the average aperture  $\bar{w}$  with distance  $\hat{x}$  from the fracture boundary: for propagation  $\bar{w} \sim \hat{x}^{1/2}$ ,  $\hat{x}^{5/8}$  and  $\hat{x}^{2/3}$  corresponding to toughness, leak-off and viscosity dominated asymptotes, respectively; while for arrest  $\bar{w} \sim \hat{x}^{1/2}$ , and recession  $\bar{w} \sim \hat{x}$ . The latter two

asymptotes share an intermediate leak-off asymptote  $\bar{w} \sim \hat{x}^{3/4}$  through the transition from arrest to recession. Moreover, using this transformation procedure we have converted the bi- and tri-process multiscale plane strain asymptotes (Detournay 2004; Garagash *et al.* 2011; Dontsov & Peirce 2015*b*; Detournay 2016; Peirce & Detournay 2022*b*) into a complete set of bi- and tri-process multiscale PKN asymptotes for propagation, arrest, and recession. These new PKN multiscale asymptotes were then used to locate the fracture free boundary in an IMMA algorithm, which was shown to provide good agreement with the solutions obtained from a multiscale planar 3-D HF model. A scaling analysis of the PKN model was used to establish the power law behaviour for the post-shut-in arrest time, length and aperture as functions of the dimensionless shut-in time  $\omega$ . These power laws were confirmed numerically using the IMMA-PKN algorithm.

Apart from its intrinsic theoretical interest, a receding PKN fracture is important to understand the dynamics of fractures with complex boundaries that have evolved in multiple sedimentary layers, but which, close to collapse, revert to receding PKN fractures confined to the injection layer (Peirce *et al.* 2024; Talebkeikhah *et al.* 2025). Thus, we have analysed the non-local PKN model to investigate the emergence of a sunset solution for receding rectangular fractures. Indeed, using a detailed asymptotic analysis of the non-local PKN model within the tip region and for points away from the tip, we established the clear sub-dominance of the dynamic terms compared with the kinematic terms in the lubrication equation. This sub-dominance leads to the fundamental dynamic-kinematic decoupling in the model equations required to establish the emergence of the sunset solution. Because of the linear tip asymptote for the aperture, a Taylor series expansion for the fracture aperture about the tip is appropriate. This series is parameterised by the decay exponent  $\gamma$  of the fracture length  $\ell$ . By choosing  $\gamma$  to be the reciprocal of the integers  $N \geq 2$ , we obtain a countable infinity of polynomial solutions of degree  $N$ . The odd integers are inadmissible as the aperture has to remain positive and, of all the even integers, the solution corresponding to smallest admissible integer  $N = 2$  is an attractor. Thus the sunset solution assumes the form

$$\bar{w}(s, t') = \hat{g}_0 t' (1 - s^2), \quad s = x/\ell, \quad \ell = \Lambda t'^{1/2}. \quad (7.1)$$

Now close to collapse  $t \gg t_0(\hat{x})$  so that  $\hat{g}_0 \approx (C'/\sqrt{t_c})$ . The dependence of the sunset solution on only the leak-off coefficient  $C_L$  is a result of the fundamental dynamic-kinematic decoupling in the model equations, which eliminates the dependence of the solution on the other parameters  $E$ ,  $\nu$ ,  $\mu$  and  $K_{Ic}$ . This isolation of the leak-off coefficient  $C_L$  in the signature of the aperture decay rate, provides an opportunity to estimate  $C_L$  from aperture measurements in laboratory experiments and in the field. Thus if one were able to measure the time derivative of  $\bar{w}$  at the injection point to yield an estimate of  $\hat{g}_0$ , we have the following estimate for  $C'$ :  $C' \approx \hat{g}_0 \times \sqrt{t_c}$ . As an illustration, an estimate of  $\hat{g}_0$  from the time derivative of one of the numerical solutions was shown to yield an estimate of  $C'$  that has an error of less than 1 %.

In this paper, numerical solutions to the non-local PKN model, which use an IMMA scheme endowed with the multiscale propagation and recession asymptotes are compared with those of a fully planar 3-D model (ILSA-PL3D), which uses the multiscale asymptotes for propagation and a minimum width constraint for recession. Since the implementation of a minimum width constraint requires the computationally intensive solution of a variational inequality at each time step, it would naturally be more efficient to model retreat of the fracture front using the recession asymptote. The recession asymptote can be used (Peirce & Detournay 2022*b*) for situations in which the aperture  $w$  is bounded below by a constant minimum aperture  $w_0$ , i.e.  $w \geq w_0$ , where the recession asymptote holds for the difference  $w - w_0$ . However, the recession asymptote was not derived for,

and has not yet been applied to, more general situations in which  $w_0$  is not likely to be constant such as closure on proppant (see Peirce *et al.* 2025).

For propagation, the non-local IMMA-PKN approximation and the ILSA-PL3D algorithm show close agreement. Indeed, despite the fact that the non-local PKN model and the ILSA-PL3D model use very different procedures to capture the fracture recession, they achieve remarkably similar results (within the constraints of the PKN geometry) essentially until the closure boundary of the ILSA-PL3D model retreats from the containment boundaries  $y = \pm H/2$ . Beyond this point of separation, the closure boundary of the ILSA-PL3D model retreats to successively shrinking ellipses that are self-similar. Cross-sections of the fracture aperture of these planar 3-D solutions also tend toward the parabolic shape characteristic of the sunset solution.

**Acknowledgements.** The author also acknowledges the assistance of Dr A. Mori of EPFL with the PyFrac runs.

**Funding.** The author acknowledges the support of the Natural Sciences and Engineering Research Council of Canada (NSERC) (grant number RGPIN-2015-06039).

**Declaration of interests.** The author reports no conflict of interest.

## Appendix A. Planar elasticity equations and reduction to plane strain

### A.1. Navier's equilibrium equation and solution in terms of Papkovitch–Neuber potentials

Consider the body force free equilibrium equations for a solid medium

$$\sigma_{ij,j} = 0, \text{ where } i, j \in \{1, 2, 3\}, \quad (\text{A1})$$

where  $\sigma_{ij}$  are the components of the Cauchy stress tensor and we adopt the Einstein summation convention over repeated indices, use the notation  $f_{,k} = \partial f / \partial x_k$ , and use the numbered coordinates to represent the cartesian coordinates  $x$ ,  $y$  and  $z$ , i.e.  $(x_1, x_2, x_3) = (x, y, z)$ . We further assume that the solid medium is isotropic and linear elastic and governed by Hooke's law

$$\sigma_{ij} = 2G\varepsilon_{ij} + \frac{2G\nu}{1-2\nu}\varepsilon_{kk}\delta_{ij}, \quad (\text{A2})$$

where  $G = E/(2(1+\nu))$  is the shear modulus,  $E$  is the Young's modulus and  $\nu$  the Poisson's ratio of the elastic medium, and the strain  $\varepsilon_{ij}$  is defined in terms of the displacement gradients to be

$$\varepsilon_{ij} = \frac{1}{2}(u_{i,j} + u_{j,i}). \quad (\text{A3})$$

Here,  $u_i$  is the component of the displacement field in the  $i$ th coordinate direction and  $u_{i,j}$  represents the derivative of  $u_i$  in the  $j$ th coordinate direction. Combining Hooke's law (A2) and the strain–displacement gradient relation (A3) to eliminate the stress tensor  $\sigma_{ij}$  from the equilibrium equations (A1), we obtain the Navier equations for the displacement field

$$\nabla^2 u_i + \frac{1}{1-2\nu}u_{j,j,i} = 0, \quad (\text{A4})$$

where, consistent with  $_{,k}$  representing a partial derivative with respect to  $x_k$ ,  $u_{j,ij} = \partial^2 u_j / (\partial x_i \partial x_j)$ . Note that summation is assumed over repeated indices. Papkovitch (1932) and Neuber (1934) obtained a general solution to the Navier equations that can be

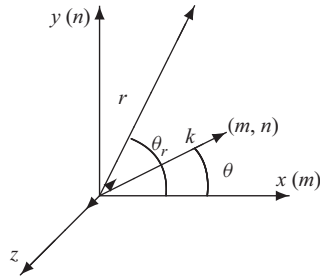


Figure 11. A point vertical displacement discontinuity in an infinite elastic medium represented by two opposing arrows indicating a point jump in the displacement component  $u_z$  at the origin  $(x, y, z) = (0, 0, 0)$ . The alternate  $m$  and  $n$  labels along the  $x$  and  $y$  axes, respectively, represent the corresponding wave numbers used in the definition of the Fourier Transform (A18). The wavenumber vector  $(m, n)$  of length  $k$  in the  $m$ – $n$  plane is used to convert the inverse transform (A23) to the Laplace transform (A24).

expressed (Crouch 1976; Kaya 1984) in terms harmonic functions  $B_i$  and  $\beta$

$$u_i = B_i - \frac{1}{4(1-\nu)}(x_k B_{k,i} + \beta)_{,i}, \quad (\text{A5})$$

where  $\nabla^2 B_i = 0$  and  $\nabla^2 \beta = 0$ . The corresponding stress components are

$$\sigma_{ij} = \frac{G}{2(1-\nu)}[(1-2\nu)(B_{i,j} + B_{j,i}) - x_k B_{k,ij} - \beta_{,ij} + 2\nu B_{k,k} \delta_{ij}]. \quad (\text{A6})$$

It can be verified that the stress field (A6) does indeed satisfy the equilibrium equation (A1).

## A.2. Solution for a point dislocation dipole in an infinite elastic medium

We now use the general solution (A5) to determine the solution to a unit dislocation dipole oriented in the  $z$  direction (see figure 11). Since  $z = 0$  is a plane of symmetry for the point dislocation dipole problem, the shear stresses along this plane must vanish, i.e.  $\sigma_{xz} = 0$  and  $\sigma_{yz} = 0$ . Since these shear stress-free conditions should hold for all points  $(x_1, x_2) = (x, y)$  within the  $z = 0$  plane, it follows that  $B_1 = 0 = B_2$  and that  $\beta_{,3} = (1-2\nu)B_3$ . Thus  $\beta$  and  $B_3$  can be expressed in terms of a single harmonic function  $\phi(x, y, z)$  as follows:

$$B_3 = -4(1-\nu)\phi_{,3} \text{ and } \beta = -4(1-\nu)(1-2\nu)\phi. \quad (\text{A7})$$

The displacement and stress components  $u_z$  and  $\sigma_{zz}$  that we shall require can now be expressed as follows:

$$u_x = (1-2\nu)\phi_{,x} + z\phi_{,xz}, \quad (\text{A8})$$

$$u_y = (1-2\nu)\phi_{,y} + z\phi_{,yz}, \quad (\text{A9})$$

$$u_z = -2(1-\nu)\phi_{,z} + z\phi_{,zz}, \quad (\text{A10})$$

$$\sigma_{xx} = 2G[\phi_{,xx} + 2\nu\phi_{,yy} + z\phi_{,xxz}], \quad (\text{A11})$$

$$\sigma_{yy} = 2G[\phi_{,yy} + 2\nu\phi_{,xx} + z\phi_{,yyz}], \quad (\text{A12})$$

$$\sigma_{zz} = 2G[-\phi_{,zz} + z\phi_{,zzz}], \quad (\text{A13})$$

$$\sigma_{xy} = 2G[(1-2\nu)\phi_{,xy} + z\phi_{,x y z}], \quad (\text{A14})$$

$$\sigma_{yz} = 2Gz\phi_{,yz}, \quad (\text{A15})$$

$$\sigma_{xz} = 2Gz\phi_{,xz}. \quad (\text{A16})$$

In order to determine the  $\phi$  field for a unit point dislocation dipole, in addition to the symmetry conditions  $\sigma_{xz} = 0 = \sigma_{yz}$ , we require that there be a unit point dislocation dipole

oriented normal to the  $z = 0$  plane

$$[u_z] = u_z(x, y, 0_+) - u_z(x, y, 0_-) = \delta(x)\delta(y)\delta(z). \quad (\text{A17})$$

Making use of the double Fourier transform

$$\hat{g}(m, n, z) = \int_{-\infty}^{\infty} \int_{-\infty}^{\infty} e^{i(mx+ny)} g(x, y, z) dx dy, \quad (\text{A18})$$

Laplace's equation  $\nabla^2 \phi = \phi_{,xx} + \phi_{,yy} + \phi_{,zz} = 0$  can be reduced to the ordinary differential equation

$$\frac{d^2 \hat{\phi}}{dz^2} - k^2 \hat{\phi} = 0, \quad (\text{A19})$$

where  $k = \sqrt{m^2 + n^2}$ . The general solution to this equation is

$$\hat{\phi}(m, n, z) = a(k)e^{-kz} + b(k)e^{+kz}, \quad (\text{A20})$$

and, excluding exponentially growing solutions, we obtain

$$\hat{\phi}(m, n, z) = \begin{cases} a_+(k)e^{-kz} & \text{for } z > 0 \\ a_-(k)e^{+kz} & \text{for } z < 0. \end{cases} \quad (\text{A21})$$

Requiring that the displacement components,  $u_x$  and  $u_y$  are continuous across the plane  $z = 0$ , it follows that  $a_+(k) = a_-(k)$  so that  $\hat{\phi}(m, n, z) = a_+(k)e^{-k|z|}$ . Now taking the Fourier transform of (A17) and matching this to the jump in the Fourier transform  $\hat{u}_z$  of  $u_z$  given in (A10), we obtain the following expression for  $\hat{\phi}$

$$\hat{\phi}(m, n, z) = \frac{1}{4(1-\nu)} \frac{e^{-k|z|}}{k}. \quad (\text{A22})$$

Inverting the Fourier transform we obtain

$$\phi(x, y, z) = \frac{1}{4(1-\nu)} \frac{1}{(2\pi)^2} \int_{-\infty}^{\infty} \int_{-\infty}^{\infty} e^{-i(mx+ny)} \frac{e^{-k|z|}}{k} dm dn. \quad (\text{A23})$$

Now introducing the polar representation  $x = r \cos \theta_r$  and  $y = r \sin \theta_r$  and  $m = k \cos \theta$  and  $n = k \sin \theta$  (see figure 11), we obtain

$$\phi(x, y, z) = \frac{1}{8\pi(1-\nu)} \int_0^{\infty} \frac{e^{-k|z|}}{k} \frac{1}{2\pi} \int_{-\pi}^{\pi} e^{-ikr \cos(\theta-\theta_r)} d\theta k dk. \quad (\text{A24})$$

Introducing the transformation  $\theta - \theta_r = t + \pi/2$ , the inner integral becomes  $1/2\pi \int_{-\pi}^{\pi} e^{ikr \sin t} dt = J_0(kr)$ , and the Laplace transform of the zeroth-order Bessel function yields

$$\phi(x, y, z) = \frac{1}{8\pi(1-\nu)} \frac{1}{\sqrt{r^2 + z^2}}. \quad (\text{A25})$$

Using the expression for  $\sigma_{zz}$  from (A13) and taking the limit  $z \rightarrow 0$ , we obtain the stress  $\sigma_{zz}(x, y, 0)$  induced at a receiving point  $(x, y)$  within the plane  $z = 0$  due to a unit

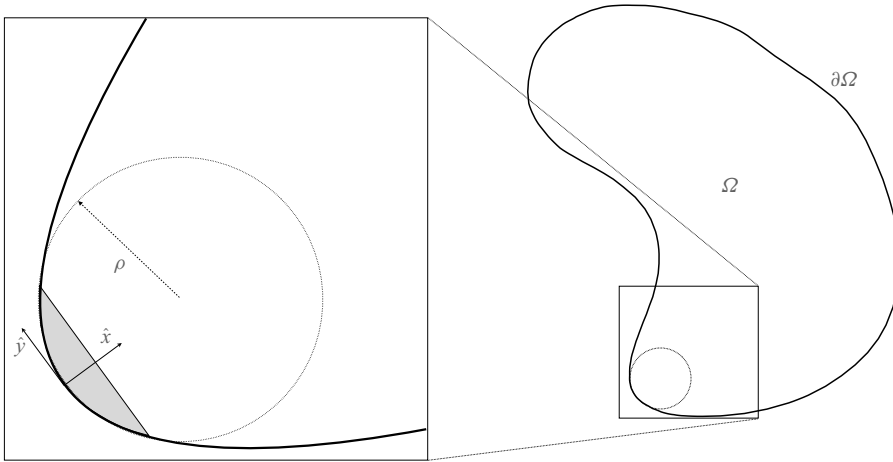


Figure 12. Plain strain limit of the planar elasticity equation: this limiting process assumes that the boundary  $\partial\Omega$  of the cracked region is sufficiently smooth (i.e. has no cusps) that a tangent circle of finite radius  $\rho$  can be constructed at any point of the boundary. At the point of contact of the circle, a local coordinate system  $(\hat{x}, \hat{y})$  is constructed such that the centre of the circle falls on the  $\hat{x}$  axis, while the  $\hat{y}$  axis is tangent to the boundary. In the limiting process the receiving point  $\hat{x}$  is taken to the boundary in such a way that  $\rho/\hat{x} \rightarrow \infty$ , which is possible because  $\rho$  is finite, and the contribution to the integral (A27) from the shaded region is estimated in order to determine the dominant behaviour of the pressure field.

dislocation dipole normal to the plane

$$\sigma_{zz} = \frac{E}{8\pi(1-\nu^2)} \frac{1}{[x^2 + y^2]^{3/2}}. \quad (\text{A26})$$

We note that if we interpreted the solution (A25) to Laplace's equation in terms of electrostatics, then  $\phi$  would represent the potential due to a point 'charge' in three dimensions in a medium with permittivity  $\epsilon = 2(1-\nu)$ , and the corresponding displacement  $u_z$  given in (A10) represents the unit dipole field oriented in the  $z$  direction.

### A.3. Plane strain limits of the planar elasticity equation

Having established the stress  $\sigma_{zz}$  (A26) due to a unit point opening discontinuity in the displacement  $u_z$  across the plane  $z=0$  and located at the origin, we are able, using the shifted coordinates  $(x' - x, y' - y)$ , to write down the integral equation relating the compressive pressure  $p(x, y)$  field at a receiving point  $(x, y)$  within the fracture consistent with the fracture aperture  $w(x, y)$  distributed within an arbitrarily shaped (including radially symmetric) planar cracked region  $\Omega$  such as that shown in 12:

$$p(x, y) = -\frac{E'}{8\pi} \int_{\Omega} \frac{w(x', y') dx' dy'}{[(x' - x)^2 + (y' - y)^2]^{3/2}}. \quad (\text{A27})$$

Equations (A1)–(A3) are consistent with tensile stresses being positive, thus, according to (A26), the point opening dislocation shown in figure 11 induces tensile stresses at all points within the plane  $z=0$  excluding the origin. Since the pressure in (A27) is positive in compression, the negative sign is required in (A27) because the integral equation is formulated in terms of pressure rather than stress, which is positive in tension.

### A.3.1. An infinitely long rectangular fracture

If we assume that in (2.2)  $\ell \gg H/2$  – to the extent that the fracture aperture in every vertical cross-section is the same, so that the elastic medium can be considered to be in a state of plane strain, then we may assume that  $w(x', y') = w(y')$  so that

$$p(x, y) = -\frac{E'}{8\pi} \int_{-H/2}^{H/2} w(y') \int_{-\ell}^{\ell} \frac{dx'}{[(x' - x)^2 + (y' - y)^2]^{3/2}} dy'. \quad (\text{A28})$$

The inner integral, in this limit, becomes  $\lim_{\ell \rightarrow \infty} \int_{-\ell}^{\ell} (dx' / [(x' - x)^2 + (y' - y)^2]^{3/2}) = 2/(y' - y)^2$ , so that (A28) is reduced to

$$p(y) = -\frac{E'}{4\pi} \int_{-H/2}^{H/2} \frac{w(y')}{(y' - y)^2} dy' = -\frac{E'}{4\pi} \int_{-H/2}^{H/2} \frac{dw(y')}{dy'} \frac{dy'}{(y' - y)}, \quad (\text{A29})$$

where the second integral results from an integration by parts and imposing the boundary conditions  $w(\pm H/2) = 0$ . We note that (A29) is equivalent to (A.7) given in (Spence & Sharp 1985).

### A.3.2. Limiting behaviour near the tip of a planar fracture with a smooth boundary

In this sub-section we outline the limiting procedure used by (Peirce & Detournay 2008) to determine the behaviour as the receiving point approaches the boundary  $\partial\Omega$  of the fractured region  $\Omega$ . We assume that  $\partial\Omega$  is sufficiently smooth that at each boundary point it is possible to define an inscribing circle of radius  $\rho$  that is tangent to  $\partial\Omega$  at the point of contact. We construct a local coordinate system  $(\hat{x}, \hat{y})$  so that  $\hat{x}$  passes through the centre of the circle and  $\hat{y}$  is tangent to the boundary (see figure 12). Locally  $\partial\Omega$  coincides with the circle  $(\hat{x} - \rho)^2 + \hat{y}^2 = \rho^2$ , which, for small  $\hat{x}$ , can be approximated by  $\hat{y}(\hat{x}) \sim \pm\sqrt{2\rho\hat{x}}$ . We now consider the local behaviour of the integral (A27) close to the tip, i.e. points for which  $\hat{x} \ll \rho$ . The dominant contribution to the pressure field in the vicinity of the tip comes from the integral over the shaded region

$$\hat{p}(\hat{x}, \hat{y}) \sim -\frac{E'}{8\pi} \int_0^a \int_{-\sqrt{2\rho\hat{x}'}}^{\sqrt{2\rho\hat{x}'}} \frac{\hat{w}(\hat{x}', \hat{y}') d\hat{y}' d\hat{x}'}{[(\hat{x}' - \hat{x})^2 + (\hat{y}' - \hat{y})^2]^{3/2}}. \quad (\text{A30})$$

Since  $\hat{w} = 0$  along  $\partial\Omega$ , as one moves away from this zero level set, the dominant increase in  $\hat{w}$  is in the direction of the  $\hat{x}$  component, normal to the boundary, while there is little variation of  $\hat{w}$  in the  $\hat{y}$  direction, which is tangent to the boundary. Thus as  $\hat{x} \rightarrow 0$  we assume that  $\hat{w}(\hat{x}', \hat{y}') \simeq \hat{w}(\hat{x}')$ . Moreover, we define a limiting process controlled by  $\hat{x}$  by scaling  $\hat{x}'$  and  $\hat{y}'$  to  $\hat{x}$ , which is the distance from the boundary to the receiving point, as follows:  $\hat{x}' = u\hat{x}$  and  $\hat{y}' = v\hat{x}$ . Thus considering the approach to the tangent point to be along the line  $\hat{y} = 0$ , the integral (A30) reduces to

$$\hat{p}(\hat{x}, 0) \sim -\frac{E'}{8\pi\hat{x}} \int_0^{a/\hat{x}} \hat{w}(u\hat{x}) \int_{-\sqrt{2u\rho/\hat{x}'}}^{\sqrt{2u\rho/\hat{x}'}} \frac{dv}{[(u-1)^2 + v^2]^{3/2}} du. \quad (\text{A31})$$

Since we are considering the limit in which the receiving point  $\hat{x}$  is much closer to the tip than the radius of curvature  $\rho$ , i.e.  $\rho/\hat{x} \rightarrow \infty$ , the inner integral becomes



$\int_{-\infty}^{\infty} (dv/[(u-1)^2 + v^2]^{3/2}) = (2/(u-1)^2)$ , so that

$$\begin{aligned}\hat{p}(\hat{x}, 0) &\sim -\frac{E'}{4\pi\hat{x}} \int_0^{a/\hat{x}} \hat{w}(u\hat{x}) \frac{du}{(u-1)^2} \\ &= -\frac{E'}{4\pi\hat{x}} \left[ -\frac{\hat{w}(u\hat{x})}{(u-1)} \Big|_0^{a/\hat{x}} + \int_0^{a/\hat{x}} \frac{d\hat{w}(u\hat{x})}{d(u\hat{x})} \frac{\hat{x} du}{(u-1)} \right].\end{aligned}\quad (\text{A32})$$

We observe that the inner integral involved in this reduction is essentially the same as the inner integral involved with the reduction of the infinitely long rectangular fracture to a single cross-section representing a fracture in a state of plane strain. Now the lower bound of the integrated term, which results from integration by parts, vanishes since  $\hat{w}(0) = 0$ , while we assume  $\hat{w}(a)$  is bounded so that the upper bound term also vanishes as  $u = a/\hat{x} \rightarrow \infty$ . Thus, taking the limit  $a/\hat{x} \rightarrow \infty$  and reverting to  $\hat{x}' = u\hat{x}$ , we obtain

$$\hat{p}(\hat{x}, 0) \sim -\frac{E'}{4\pi} \int_0^{\infty} \frac{d\hat{w}(\hat{x}')}{d\hat{x}'} \frac{d\hat{x}'}{(\hat{x}' - \hat{x})}, \quad (\text{A33})$$

which is the elasticity equation for a semi-infinite fracture in a state of plane strain.

#### A.4. Semi-infinite crack eigenfunction and the Sneddon solution

##### A.4.1. Semi-infinite crack eigenfunction

If we consider power law fracture apertures of the form  $\hat{w} = \hat{x}^\lambda$ , where  $0 < \lambda < 1$  then (A33) becomes

$$\hat{p}(\hat{x}, 0) \sim -\frac{E'\lambda}{4\pi} \int_0^{\infty} \frac{\hat{x}'^{\lambda-1}}{(\hat{x}' - \hat{x})} d\hat{x}'. \quad (\text{A34})$$

Now introducing a branch cut along the ray  $[0, \infty)$ , integrating along the keyhole contour centred at the branch point  $\hat{x}' = 0$  and evaluating the residue contributions either side of the branch cut, we obtain

$$\hat{p}(\hat{x}, 0) \sim -\frac{E'\lambda}{4\pi} (-\pi \cot(\pi\lambda) \hat{x}^{\lambda-1}) = \frac{E'\lambda}{4} \cot(\pi\lambda) \hat{x}^{\lambda-1} \quad (\text{A35})$$

i.e. the Cauchy operator (A33) has an eigenfunction  $\hat{x}^{\lambda-1}$  with eigenvalue  $-(E'\lambda/4) \cot(\pi\lambda)$ . This result is also established in appendix C of (Spence & Sharp 1985).

##### A.4.2. The Sneddon solution

The solution (Sneddon 1995) to the plane strain integral equation (A29), relating the applied pressure  $p(y)$  to the fracture aperture  $w(y)$ , can be solved directly for the special case  $p(y) = p_0$  by making use of the following property of the Chebychev polynomials of the second kind  $U_n(x)$ :

$$\int_{-1}^1 \frac{U_n(t) \sqrt{1-t^2}}{(t-x)^2} dt = -\pi(n+1)U_n(x), \quad (\text{A36})$$

where  $U_n(\cos \theta) \sin \theta = \sin((n+1)\theta)$  and  $x = \cos \theta$ . Since  $U_0(x) = 1$ , when we combine this property with (A29), we obtain

$$w(y) = \frac{4}{E'} p_0 \left( \frac{H}{2} \right) \sqrt{1 - (2y/H)^2}. \quad (\text{A37})$$

More generally, (A29) can be written succinctly (Spence & Sharp 1985; Lister 1990) in terms of the Hilbert transform  $\mathcal{H}(f) = (1/\pi) \int_{-\infty}^{\infty} (f(\eta)/(\eta - y)) d\eta$  as follows:

$$p(y) = -\frac{E'}{4} \mathcal{H} \left( \frac{dw}{dy'} \right). \quad (\text{A38})$$

Here, the finite crack is enforced by the condition that  $w(y) = 0$  for  $|y| \geq H/2$ . Since  $\mathcal{H}(\mathcal{H}(\cdot)) = -I$ , taking the Hilbert transform (Lister 1990) we obtain

$$\frac{dw}{dy} = \frac{4}{E'} \mathcal{H}(p) = \frac{4}{E' \pi} \int_{-a}^a p(y') \left( \frac{a^2 - y'^2}{a^2 - y^2} \right)^{1/2} \frac{dy'}{y' - y} + \frac{C}{\sqrt{a^2 - y^2}}, \quad (\text{A39})$$

where  $a = H/2$ . For the special case of a constant pressure  $p(y') = p_0$  within the vertical cross-section, using the integral  $\int_{-1}^1 \sqrt{(1-t^2)/(t-y)} dt = -\pi y$ , integrating and imposing the boundary conditions  $w(\pm H/2) = 0$ , we obtain (A37). Integrating (A37) over the vertical cross-section of the rectangular fracture  $(-H/2, H/2)$  we obtain the local pressure-width (2.10).

#### REFERENCES

- ADACHI, J.I. 2001 Fluid-driven fracture in permeable rock. PhD Thesis, University of Minnesota.
- ADACHI, J.I., SIEBRITS, E., PEIRCE, A. & DESROCHES, J. 2007 Computer simulation of hydraulic fractures. *Intl J. Rock Mech. Mining Sci.* **44**, 739–757.
- ADACHI, J.I. & DETOURNAY, E. 2008 Plane strain propagation of a hydraulic fracture in a permeable rock. *Eng. Fract. Mech.* **75**, 4666–4694.
- ADACHI, J.I., DETOURNAY, E. & PEIRCE, A. 2010 An analysis of classical pseudo-3D model for hydraulic fracture with equilibrium height growth across stress. *Intl J. Rock Mech. Mining Sci.* **47**, 625–639.
- ADACHI, J. & PEIRCE, A.P. 2008 Asymptotic analysis of an elasticity equation for a finger-like hydraulic fracture. *J. Elasticity* **90**, 43–69.
- BOLZON, G. & COCHETTI, G. 2003 Direct assessment of structural resistance against pressurized fracture. *Intl J. Numer. Anal. Meth. Geomech.* **27**, 353–378.
- BUNGER, A.P. & DETOURNAY, E. 2008 Experimental validation of the tip asymptotics for a fluid-driven crack. *J. Mech. Phys. Solids* **56**, 3101–3315.
- BUNGER, A.P., LAU, H., WRIGHT, S. & SCHMIDT, H. 2023 Mechanical model for geomechanical pumped storage in horizontal fluid-filled lenses. *Intl J. Numer. Anal. Meth. Geomech.* **47**, 1349–1372.
- CARTER, E.D. 1957 Optimum fluid characteristics for fracture extension. In *Drilling and Production Practices* (ed. G.C. HOWARD & C.R. FAST), pp. 261–270, American Petroleum Institute.
- CROUCH, S.L. 1976 *Analysis of Stresses and Displacements Around Underground Excavations: an Application of the Displacement Discontinuity Method*, Geomechanics Report to the National Science Foundation. University of Minnesota.
- CROUCH, S.L. & STARFIELD, A.M. 1983 *Boundary Element Methods in Solid Mechanics*. George Allen and Unwin.
- DE PATER, H., DESROCHES, J., GROENENBOOM, J. & WEIJERS, L. 1996 Physical and numerical modeling of hydraulic fracture closure. *SPE Prod. Facilities* **11** (02), 122–128.
- DESROCHES, J., DETOURNAY, E., LENOACH, B., PAPANASTASIOU, P., PEARSON, J.R.A., THIERCELIN, M. & CHENG, A.H.D. 1994 The crack tip region in hydraulic fracturing. *Proc. R. Soc. Lond. A* **447**, 39–48.
- DESROCHES, J. & THIERCELIN, M. 1993 Modelling the propagation and closure of microhydraulic fractures. *Intl J. Rock Mech. Mining Sci.* **30** (7), 1231–1234.
- DETOURNAY, E. 2004 Propagation regimes of fluid-driven fractures in impermeable rocks. *Intl J. Geomech.* **4** (1), 1–11.
- DETOURNAY, E. 2016 Mechanics of hydraulic fractures. *Annu. Rev. Fluid Mech.* **48**, 311–339.

- DETOURNAY, E. & PEIRCE, A. 2014 On the moving boundary conditions for a hydraulic fracture. *Intl J. Eng. Sci.* **84**, 147–155.
- DONTSOV, E.V. 2016 An approximate solution for a penny-shaped hydraulic fracture that accounts for fracture toughness, fluid viscosity and leak-off. *R. Soc. Open Sci.* **3**, 160737.
- DONTSOV, E.V. 2017 An approximate solution for a plane strain hydraulic fracture that accounts for fracture toughness, fluid viscosity, and leak-off. *Intl J. Fract.* **205**, 221–237.
- DONTSOV, E.V. 2022 Analysis of a constant height hydraulic fracture, and leak-off, mechanics of hydraulic fractureing: experiment, model, and monitoring, 127–139.
- DONTSOV, E. & PEIRCE, A. 2015a An enhanced pseudo-3D model for hydraulic fracturing accounting for viscous height growth, non-local elasticity, and lateral toughness. *Eng. Fract. Mech.* **42**, 116–139.
- DONTSOV, E. & PEIRCE, A. 2015b A non-singular integral equation formulation to analyse multiscale behaviour in semi-infinite hydraulic fractures. *J. Fluid Mech.* **781**, R1.
- DONTSOV, E. & PEIRCE, A. 2016 Comparison of toughness propagation criteria for blade-like and pseudo-3D hydraulic fractures. *Eng. Fract. Mech.* **160**, 238–247.
- DONTSOV, E.V. & PEIRCE, A. 2017 A multiscale implicit Level Set Algorithm (ILSA) to model hydraulic fracture propagation incorporating combined viscous, toughness, and leak-off asymptotics. *Comput. Meth. Appl. Mech. Eng.* **313**, 53–84.
- ECONOMIDES, M.J. & NOLTE, K.G. 2000 *Reservoir Stimulation*. John Wiley & Sons.
- GARAGASH, D.I. & DETOURNAY, E. 2000 The tip region of a fluid-driven fracture in an elastic medium. *ASME J. Appl. Mech.* **67** (1), 183–192.
- GARAGASH, D.I. 2006 Plane-strain propagation of a fluid-driven fracture during injection and shut-in: asymptotics of large toughness. *Eng. Fract. Mech.* **73**, 456–481.
- GARAGASH, D.I., DETOURNAY, E. & ADACHI, J.I. 2011 Multiscale tip asymptotics in hydraulic fracture with leak-off. *J. Fluid Mech.* **669**, 260–297.
- HAIMSON, B.C. 1989 Hydraulic fracturing stress measurements, special issue. *Intl J. Rock Mech. Mining Sci. Geomech. Abstr.* **26**, 447–485.
- HAYASHI, K. & HAIMSON, B.C. 1991 Characteristics of shut-in curves in hydraulic fracturing stress measurements and determination of in situ minimum compressive stress. *J. Geophys. Res.: Solid Earth* **96** (B11), 18311–18321.
- HILLS, D.A., KELLY, P.A., DAI, D.N. & KORSUNSKY, A.M. 1996 Solution of crack problems, the distributed dislocation technique. In *Solid Mechanics and Its Applications*, vol. 44. Kluwer Academic Publisher.
- KAYA, A.C. 1984 Applications of integral equations with strong singularities in fracture mechanics. *PhD Thesis*, Lehigh University, USA.
- KEMP, L.F. 1989 Study of Nordgren's equation of hydraulic fracturing. In *SPE Joint Rocky Mountain Regional/Low Permeability Reservoirs Symposium and Exhibition*, pp. 608. The Society of Petroleum Engineers.
- KHRISTIANOVIC, S.A. & ZHELTOV, Y.P. 1955 Formation of vertical fractures by means of highly viscous liquid. In *Proceedings of the Fourth World Petroleum Congress, Rome*, pp. 579–586. World Petroleum Congress.
- KANIN, E.A., GARAGASH, D.I. & OSIPTSOV, A.A. 2020 The near-tip region of a hydraulic fracture with pressure-dependent leak-off and leak-in. *J. Fluid Mech.* **892**, A31.
- KANIN, E.A., DONTSOV, E.V., GARAGASH, D.I. & OSIPTSOV, A.A. 2020 A radial hydraulic fracture with pressure-dependent leak-off. *J. Mech. Phys. Solids* **143**, 104062.
- KOVALYSHEN, Y. & DETOURNAY, E. 2010 A reexamination of the classical PKN model of hydraulic fracture. *Transp. Porous Med.* **81** (2), 317–339.
- LAKIROUHANI, A., DETOURNAY, E. & BUNGER, A. 2016 A reassessment of in situ stress determination by hydraulic fracturing. *Geophys. J. Intl.* **205**, 1859–1873.
- LECAMPION, B. *et al.* 2013 The impact of the near-tip logic on the accuracy and convergence rate of hydraulic fracture simulators compared to reference solutions, Chapter 43. In *Effective and Sustainable Hydraulic Fracturing*, p. 1000. InTech.
- LENOACH, B. 1995 The crack tip solution for hydraulic fracturing in a permeable solid. *J. Mech. Phys. Solids* **43**, 1025–1043.
- LISTER, J.R. 1990 Buoyancy-driven fluid fracture: similarity solutions for the horizontal and vertical propagation of fluid-filled cracks. *J. Fluid Mech.* **217**, 213–239.
- MADYAROVA, M. 2003 Fluid-driven penny-shaped fracture in permeable rock, M.Sc. Thesis, University of Minnesota, USA.
- MCCLURE, M.W. & HORNE, R.N. 2013 *Discrete Fracture Network Modeling of Hydraulic Stimulation: Coupling Flow and Geomechanics, Springer Briefs in Earth Sciences*. Springer.

- MOHAMMADNEJAD, T. & ANDRADE, J.E. 2016 Numerical modeling of hydraulic fracture propagation, closure and reopening using XFEM with application to in-situ stress estimation. *Intl J. Numer. Anal. Meth. Geomech.* **40** (15), 2033–2060.
- MORI, A. & LECAMPION, B. 2021 Arrest of a radial hydraulic fracture upon shut-in of the injection. *Intl J. Solids Struct.* **219–220**, 133–120.
- MORI, A., PERUZZO, C., GARAGASH, D. & LECAMPION, B. 2024 How stress barriers and fracture toughness heterogeneities arrest buoyant hydraulic fractures. *Rock Mech. Rock Eng.* **5**, 1–27.
- NEUBER, H. 1934 Ein neuer ansatz zur losung raumlicher probleme der elastizitatstheorie. *Z. Angew. Math. Mech.* **14**, 203–212.
- NOLTE, K.G. 1979 Determination of fracture parameters from fracturing pressure decline. In *Proceeding of SPE Annual Technology Conference and Exhibition, Las Vegas, SPE 8341*. Society of Petroleum Engineers.
- NOLTE, K.G. 1991 Fracturing-pressure analysis for nonideal behavior. *J. Petrol Technol.* **43**, 210–218.
- NORDGREN, R.P. 1972 Propagation of vertical hydraulic fractures. *J. Petrol Technol.* **1972**, 306–314.
- PAPKOVICH, P.F. 1932 Solution generale des equations differentielles fondamentales de l’elasticite, exprimee par trois fonctions harmoniques. *C. R. Acad. Sci.* **195**, 513–515.
- PEIRCE, A. & DETOURNAY, E. 2008 An implicit level set method for modeling hydraulically driven fractures. *Comput. Meth. Appl. Mech. Eng.* **197**, 2858–2885.
- PEIRCE, A. 2015 Modeling multi-scale processes in hydraulic fracture propagation using the implicit level set algorithm. *Comput. Meth. Appl. Mech. Eng.* **283**, 881–908.
- PEIRCE, A. 2016 Implicit level set algorithms for modelling hydraulic fracture propagation. *Phil. Trans. R. Soc. A. Phil. Trans. R. Soc. A.* **374**, 20150423.
- PEIRCE, A. & DETOURNAY, E. 2022a Sunset similarity solution for a receding hydraulic fracture. *J. Fluid Mech.* **944**, A7.
- PEIRCE, A. & DETOURNAY, E. 2022b Multiscale tip symptotics for a deflating hydraulic fracture with leak-off. *J. Fluid Mech.* **947**, A17.
- PEIRCE, A. & DETOURNAY, E. 2022c The arrest and recession dynamics of a deflating hydraulic fracture in a permeable elastic medium in a state of plane strain. *Intl J. Solids Struct.* **254–255**, 111906.
- PEIRCE, A. 2022 The arrest and recession dynamics of a deflating radial hydraulic fracture in a permeable elastic medium. *J. Mech. Phys. Solids* **166**, 104926.
- PEIRCE, A., ABBAS, S. & DETOURNAY, E. 2024 The sunset solution: closure on leaking proppant, ARMA. In *Proceeding of the 58TH US Rock Mechanics-Geomechanics Symposium*, pp. 24-0428.
- PEIRCE, A., ABBAS, S. & DETOURNAY, E. 2025 The sunset solution: closure on leaking proppant. *Rock Mech. Rock Eng.* <https://doi.org/10.1007/s00603-025-04747-7>
- PENMAN, A.D.M. 1977 The failure of the Teton dam. *Ground Eng.* **10** (6), 18–27.
- PERKINS, T.K. & KERN, L.R. 1961 Widths of hydraulic fractures. *J. Petrol. Tech.* **13**, 937–949.
- PERUZZO, C. 2023 Three-dimensional hydraulic fracture propagation in homogeneous and heterogeneous media, PhD thesis, EPFL Lausanne.
- PRICHARD, D., WOODS, A.W. & HOGG, A.J. 2001 On the slow draining of a gravity current moving through a layered permeable medium. *J. Fluid Mech.* **444**, 23–47.
- RICE, J.R. Mathematical Analysis in the Mechanics of Fracture. In *Fracture, an Advanced Treatise* (ed. H.LIEBOWITZ), vol. **II**, chap. 3, pp. 191–311. Academic Press.
- ROPER, S.M. & LISTER, J.R. 2007 Buoyancy-driven crack propagation: the limit of large fracture toughness. *J. Fluid Mech.* **580**, 359–380.
- SARVARAMINI, E. & GARAGASH, D. 2015 Breakdown of a pressurized fingerlike crack in a permeable solid. *J. Appl. Mech.* **82**, 061006.
- SAVITSKI, A. & DETOURNAY, E. 2002 Propagation of a fluid-driven penny-shaped fracture in an impermeable rock: asymptotic solutions. *Intl J. Solids Struct.* **39**, 6311–6337.
- SNEDDON, I.N. 1995 *Fourier transforms*. Dover.
- SPENCE, D.A. & SHARP, P. 1985 Self-similar solutions for elastohydrodynamic cavity flow. *Proc. R. Soc. Lond.A* **400**, 289–313.
- TALEBKKEIKHAH, M., MORI, A., PEIRCE, A., LECAMPION, B. & DETOURNAY, E. 2025 Numerical modeling of the recession and closure of planar three-dimensional hydraulic fractures: contact-based versus asymptotic-informed schemes. *Intl J. Num. Anal. Meth. Geomech.* (Under review).
- TSAI, V.C. & RICE, J.R. 2010 A model for turbulent hydraulic fracture and application to crack propagation at glacier beds. *J. Geophys. Res. Earth Surf.* **115** (F3), 0148–0227.
- VAN AS, A. & JEFFREY, R.G. 2000 *Caving Induced by Hydraulic Fracturing at North Parkes Mines*. Pacific Rocks.
- VAN DAM, D.B., DE PATER, C.J. & ROMIJN, R. 2000 Analysis of hydraulic fracture closure in laboratory experiments. *SPE Prod. Facilities* **15** (03), 151–158.

- ZANGANEH, B., CLARKSON, C.R. & HAWKES, R.V. 2017 Reinterpretation of fracture closure dynamics during diagnostic fracture injection tests. In *Proceedings of SPE Annual Technical Conference and Exhibition*, The Woodlands.
- ZARRINDERAKHT, M., SCHOOF, C. & PEIRCE, A. 2022 The effect of hydrology and crevasse wall contact on calving. *The Cryosphere* **22**, 4491–4512.
- ZARRINDERAKHT, M., SCHOOF, C. & PEIRCE, A. 2024 An analysis of the interaction between surface and basal crevasses in ice shelves. *The Cryosphere* **18**, 3841–3856.
- ZIA, H. & LECAMPION, B. 2020 PyFrac: a planar 3D hydraulic fracture simulator. *Comput. Phys. Commun.* **255**, 107368.